Royal Netherlands Institute for Sea Research

This is a pre-copyedited, author-produced version of an article accepted for publication, following peer review.

Kraal, P.; van Genuchten, C.M.; Lenstra, W.K. & Behrends, T. (2020). Coprecipitation of phosphate and silicate affects environmental iron (oxyhydr)oxide transformations: A gel-based diffusive sampler approach. *Environmental Science and Technology*, 54, 12795-12802

Published version: https://dx.doi.org/10.1021/acs.est.0c02352

NIOZ Repository: http://imis.nioz.nl/imis.php?module=ref&refid=330302

[Article begins on next page]

1 # Coprecipitation of phosphate and silicate affects

2 # environmental iron (oxyhydr)oxide transformations:

3 # a gel-based diffusive sampler approach

4 *Peter Kraal*[†§], Case M. van Genuchten[†], Wytze K. Lenstra[†], Thilo Behrends[†]*

5 [†] Department of Earth Sciences – Geochemistry, Faculty of Geosciences, Utrecht University, PO

6 Box 80021, 3508 TA Utrecht, The Netherlands

7 [§] Royal Netherlands Institute for Sea Research, Department of Ocean Systems, and Utrecht

8 University, PO Box 59, 1790 AB Den Burg, The Netherlands

9 * Corresponding author, peter.kraal@nioz.nl

11

12

ABSTRACT

Sorption of nutrients such as phosphate (P) and silicate (Si) by ferric iron (oxyhydr)oxides

(FeOx) modulates nutrient mobility and alters the structure and reactivity of the FeOx. We

investigated the impact of these interactions on FeOx transformations using a novel approach

with samplers containing synthetic FeOx embedded in diffusive hydrogels. The FeOx were

prepared by Fe(III) hydrolysis and Fe(II) oxidation, in the absence and presence of P or Si.

Coprecipitation of P or Si during synthesis altered structure of Fe precipitates and, in case of

Fe(II) oxidation, lepidocrocite was (partly) substituted by poorly ordered FeOx. The pure and P-

or Si-bearing FeOx were deployed in (i) freshwater sediment rich in dissolved Fe(II) and P and

(ii) marine sediment with sulfidic pore-water. Iron(II)-catalyzed crystallization of poorly ordered

FeOx was negligible, likely due to surface passivation by adsorption of dissolved P. Reaction

with dissolved sulfide was modulated by diffusion limitations and therefore the extent of

sulfidation was lowest for poorly ordered FeOx with high reactivity towards sulfide that created

temporary, local sulfide depletion (Fh < Lp). We show that coprecipitation-induced changes in

FeOx structure affect coupled iron-nutrient cycling in aquatic ecosystems. The gel-based method

enriches our geochemical toolbox by enabling detailed characterization of target phases under

natural conditions.

INTRODUCTION

Poorly crystalline ferric iron (oxyhydr)oxides (FeOx) have high sorption capacity and therefore modulate the mobility and bioavailability of (trace) contaminants and nutrients in aquatic systems. Furthermore, laboratory studies have shown that adsorption or coprecipitation of such species can alter the transformation and dissolution of FeOx such as ferrihydrite (Fh) and lepidocrocite (Lp). Strong effects have been observed in laboratory studies for nutrients such as phosphate (PO_4, denoted here as P) and silicate (SiO_4, denoted here as Si).[1-6]

Occupation of FeOx surface sites by oxyanions such as PO_4 or SiO_4 during Fe precipitate formation decreases structural order. The extent of the impact depends on the molar oxyanion/Fe ratio and the FeOx formation pathway. Sorption of oxyanions during Fe(III) hydrolysis and Fe(II) oxidation disrupts Fe-Fe polymerization and under high oxyanion/Fe ratios, amorphous precipitates such as Fe(III) phosphate can form.[7-8] Furthermore, in the case of Fe(II) oxidation, sorption of oxyanions inhibits Fe(II)-catalyzed transformation of freshly formed nano-scale FeOx into more crystalline Fe phases.[3, 7-10] The environmental implications of these FeOx alterations are poorly known. In particular, it is unclear how key FeOx transformation pathways such as crystallization and sulfidation are affected under natural conditions. These transformations alter the nutrient and contaminant sorption capacity of Fe minerals and represent key processes in the coupling between nutrient dynamics and Fe redox cycling and transformation.[11-13]

Detailed tracking of the environmental fate of target Fe phases can be complicated by interference from a large and diverse pool of background Fe in natural sediments. Laboratory-based batch and column experiments[14-18] have provided detailed insight into FeOx transformations but may not adequately represent natural conditions, in part because of the use of FeOx as single solid phase or synthetic sediment. Here, we aim to advance our understanding of the environmental

3

58 fate of Fe by adapting an established pore-water method (diffusive gradients/equilibrium in thin

59 films, DGT-DET)[19-20] to deploy well-characterized (P-bearing) FeOx, embedded in diffusive

60 hydrogels, in natural sediments. We show that the target FeOx undergo geochemical

61 transformations (with a prominent role for P and Si coprecipitation) that can be investigated in

62 (micro-scale) detail because the hydrogels only contain FeOx and its transformation products.

63

64 **MATERIALS AND METHODS**

65 **Synthesis of iron precipitates.** Two-line ferrihydrite (Fh; $Fe(II)_{10}O_{14}(OH)_2 \cdot nH_2O$ with $n < 1$)[21-

66 22] and lepidocrocite (Lp; $\gamma\text{-}Fe(III)OOH$), referred to here as 'pure' FeOx, were prepared following

67 established protocols using Fe(III) hydrolysis for Fh synthesis and Fe(II) oxidation for Lp synthesis

68 at circumneutral pH (7–8).[23] Base hydrolysis of a concentrated Fe(III) solution is a widely used

69 method to synthesize Fh-type precipitates representative of poorly ordered FeOx in natural soils

70 and sediments. Such precipitates form in anthropogenic landscapes by neutralization of acidic,

71 Fe(III)-rich drainage from acid sulfate soils and mine tailings, where the FeOx play an important

72 role in scavenging contaminants.[24-27] Lepidocrocite from oxidation of a concentrated Fe(II)

73 solution serves as analog for more crystalline natural FeOx formed around redox interfaces in

74 natural soils and sediments where initial poorly ordered FeOx precipitates undergo further

75 crystallization by reaction with Fe(II).[13, 28-29]

76 In addition to pure FeOx, we prepared FeOx with coprecipitated P or Si at a molar (P, Si)/Fe

77 ratio of 0.1. A P/Fe ratio of 0.1 is representative of the ratio between Fe(III) and associated P in

78 oxic surface sediments.[30-32] Furthermore, previous studies have elucidated in detail the impact of

79 P and Si coprecipitation on FeOx structure at similar oxyanion/Fe ratios.[3, 7, 10] The FeOx prepared

80 by Fe(III) hydrolysis and Fe(II) oxidation are referred to as $FeOx_{hydr}$ and $FeOx_{oxid}$, respectively.

81   Details on FeOx synthesis are given in the Supporting Information and have been reported

82   previously.[6]

83

84   **Preparation of (FeOx-bearing) hydrogels and samplers.** Several types of (bis)acrylamide-

85   cross linked hydrogels were prepared. Using existing protocols, DET (diffusive equilibrium in thin

86   films[19]) hydrogels were prepared for measurement of pore-water Fe(II)[33] and P[34] and DGT

87   (diffusive gradients in thin films) binding hydrogels were prepared for pore-water sulfide.[35] Using

88   an adapted protocol (see Supporting Information), FeOx-bearing thin film (FeOx-BT) hydrogels

89   were prepared by adding small aliquots of FeOx in suspension during hydrogel casting. Diffusive

90   samplers for pore-water analysis or FeOx deployment were prepared by placing DGT-DET or

91   FeOx-BT hydrogels, covered with filter membrane, in rigid Teflon[TM] samplers (DGT Research,

92   Lancaster) as detailed in the Supporting Information. The FeOx-BT samplers allow diffusive

93   exchange with pore-water but prevent direct physical contact between the target FeOx and solid-

94   phase sediment (i.e. contamination).

95

96   **Deployment of hydrogel samplers.** Samplers were deployed during the summer period (June

97   - September) of 2016 at two contrasting sites in The Netherlands. Site 1 was a freshwater drainage

98   ditch on the Utrecht University campus (52°5.27' N, 5°9.80' E) with clayey to sandy sediment rich

99   in dissolved Fe(II) and P. Site 2 was a tidal mud flat with sulfidic silty to sandy sediment in the

100   marine Oosterschelde estuary (salinity 28 PSU) in the southwest of The Netherlands (51°26.35'

101   N, 4°9.87' E). Site 1 was used to investigate Fe(II)-catalyzed transformation of Fh and Site 2 was

102   used to study Fh and Lp sulfidation. At each site, DGT-DET and FeOx-BT samplers were

103   introduced into the sediment. Pore-water samplers were left overnight, the FeOx were deployed

104   for four weeks. Details on deployment and recovery of the samplers are given in the Supporting

105   Information. We conducted an additional short-term FeOx sulfidation experiment under controlled

106   conditions. For this laboratory-based experiment, a microcosm of surface sediment with 5 cm of

107   overlying water was created using mixed surface sediment (top 10 cm) and unfiltered seawater

108   from Site 2. These benthic microcosms were left to equilibrate at room temperature for a week

109   while the overlying water was kept O_2-saturated by bubbling air through it. Subsequently, pore-

110   water samplers and FeOx-BT samplers were inserted and left overnight.

111   In the field and laboratory experiments, the DGT-DET pore-water samplers were deployed in

112   sets of two to measure ΣH_2S (DGT) and Fe (DET) or ΣH_2S (DGT) and P (DET). During the field

113   experiments, we deployed duplicate samplers for each type of FeOx-BT hydrogel were deployed.

114   In the laboratory sulfidation experiment, single samplers for each type of FeOx-BT hydrogel were

115   used.

116

117   **Processing of DET-DGT and FeOx-BT hydrogels.** The pore-water DGT and DET

118   hydrogels were analyzed as described previously (also see Supporting Information). Briefly, DET

119   hydrogels that had equilibrated with pore-water were overlain with a DET hydrogel that had

120   equilibrated with a solution containing reagent for spectrophotometric detection of either Fe(II)

121   (Ferrozine[TM]) or P (molybdate blue). Color formation by diffusive exchange between the sample

122   and staining gels was quantified and converted into dissolved Fe(II) or P concentration.[33-34] In

123   DGT gels, sulfide is bound as black-colored Ag_2S which stains the initially white gel. From the

124   intensity of this color change, the dissolved sulfide concentration can be calculated.[35]

125   The FeOx-BT hydrogels were removed from the samplers in an Ar-filled anoxic glovebox. One

126   of the duplicate gels was immediately cut horizontally in four equal pieces of ~ 3.5 cm length and

127   1.5 cm width. These gel cuts were shortly stored in anoxic milliQ (with two water changes to

128   remove any dissolved components) prior to further preparation for X-ray analysis. The second

129   duplicate gel was stored intact in Ar-purged anoxic milliQ. A selection of these duplicate gels (Fh,

130   P9-FeOx$_{hydr}$, Si9-FeOx$_{hydr}$) were cut as described above and used for micro-scale XRF (µXRF)

131   scanning.

132

133   **Micro-scale XRF and synchrotron-based XAS analysis of hydrogel sections.** Detailed

134   descriptions of sample preparation and analysis for micro-XRF and XAS analysis are given in the

135   Supporting Information. Briefly, for µXRF analysis, selected duplicate wet gel cuts were placed

136   on microscope slides and vertical line scans were collected at 30 µm resolution for Fe, P and S.

137   For synchrotron-based X-ray absorption spectroscopy (XAS), samples were freeze-dried, ground

138   and mixed with cellulose and pressed into pellets that were used for Fe K-edge XAS analysis at

139   beamline BM26A (DUBBLE) of the European Synchrotron Radiation Facility (ESRF) in

140   Grenoble, France. Details on the beamline setup can be found in Nikitenko et al.[36] Spectra were

141   recorded at room temperature in transmission mode from 6962 to 7862 eV, corresponding to a

142   maximum k of 13 Å^{-1} in the EXAFS region. For each sample, two spectra were collected and

143   merged. Repeated measurement of an FeS-rich sample showed no sign of oxidation or beam

144   damage during analysis. Data normalization was done using the Athena software package.[37] Iron

145   speciation was obtained by linear combination fitting of components (representing Fe phases)

146   extracted from the entire XAS dataset (24 spectra including references) by iterative transform

147   factor analysis using the ITFA software package.[38] Analysis was performed in k space, using a

148   fitting window of k = 2 - 11 Å^{-1} of the k^3 weighted EXAFS spectra. For sulfidation samples, the

149   degree of Fe sulfidation (DOS)[39] was determined as the fraction of total Fe transformed into iron

150   (mono)sulfide based on the results from the LCF.
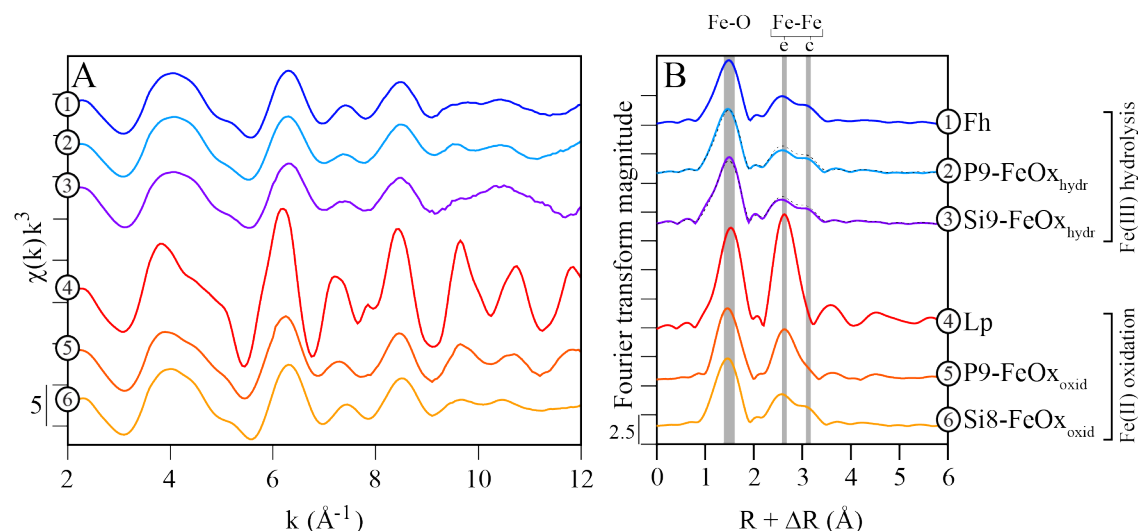

151

Figure 1. (A) Fe K-edge EXAFS spectra and (B) Fourier-transformed Fe K-edge EXAFS spectra of FeOx synthesized for this study. Vertical grey bands in (B) mark magnitude peaks arising from Fe - O bonds and edge-sharing (e) and corner-sharing (c) Fe octahedra. In (B), dashed black lines plotted with spectrum 2 and 3 show the Fh spectrum for reference.

152

RESULTS AND DISCUSSION

154   **Structure of the initial FeOx.** Hydrolysis of concentrated Fe(III) solutions formed Fh-type

155   precipitates (Fig. 1). During Fe(III) hydrolysis in the presence of 10 mol% dissolved P or Si relative

156   to Fe, the poorly ordered FeOx that formed contained 9 mol% P (P9-FeOx$_{hydr}$) or Si (Si9-FeOx$_{hydr}$).

157   The FeOx$_{hydr}$ with coprecipitated P and Si showed slightly less amplitude in the second and third

158   peak in the Fourier-transformed (FT) spectra (R + ΔR = 2.4 and 3.1 Å) that represent edge- and

159   corner-sharing Fe octahedra. This may reflect inhibition of Fe polymerization and formation of

160   aggregates of Fe oligomers linked by P or Si. This impact of strongly-sorbing oxyanions such as

161   phosphate, silicate and arsenate on FeOx formation from Fe(III) hydrolysis has been described in

162 detail in previous work.[6, 9-10] The small decrease in peak amplitude under the current experimental

163 conditions at P/Fe = 0.1 suggests that inhibition of Fe polymerization was minor under the current

164 experimental conditions.

165 For Fe precipitates from Fe(II) oxidation, the impact of P or Si coprecipitation at an initial P/Fe

166 ratio of 0.1 (10 mol% P relative to Fe) was more profound. In the absence of dissolved P or Si,

167 pure Lp formed because freshly formed nano-scale FeOx undergoes rapid Fe(II)-catalyzed

168 transformation.[23] The Lp showed a strongly developed second-shell Fe peak at ~2.6 Å (uncorrected

169 for phase shift) in the FT spectrum arising from edge-sharing Fe(III) octahedra (Fig. 1B). The FT

170 spectrum of P9-FeOx$_{oxid}$ (9 mol% P relative to Fe) was markedly different with decreased

171 amplitudes of the Fe-O and edge-sharing Fe peaks. The P9-FeOx$_{oxid}$ spectrum represents a mixture

172 of Fe phases, resulting from sequential formation of Fe precipitates by Fe(II) oxidation in the

173 presence of dissolved P.[7-8] Initially, highly disordered Fe(III)-P polymers and/or P-rich hydrous

174 ferric oxide (P-HFO) form and rapidly deplete dissolved P. The Fe(III) that is subsequently formed

175 under P-depleted conditions partly contributes to polymerization of Fe(III)-P into P-HFO and

176 partly precipitates as Lp. Previous work indicates that under the current experimental conditions

177 (P/Fe = 0.1), Fe precipitates most likely consist of a mixture of highly disordered P-HFO and Lp.[8]

178 The LCF results showed that P9-FeOx$_{oxid}$ could be reproduced as a combination of P-HFO (70 %)

179 and Lp (30%). Assuming all P was associated with the P-HFO fraction, this precipitate would have

180 a molar P/Fe ratio of ~ 0.13. The fraction of P-HFO was likely overestimated in the LFC procedure

181 and therefore the P/Fe of the P-HFO would have been underestimated.

182 Dissolved Si has a lower affinity for Fe(III) and does not become depleted but rather

183 coprecipitates with FeOx precipitates throughout FeOx synthesis, thereby shifting the reaction

184 product of Fe(II) oxidation from Lp to Si-HFO.[3, 7] Our results showed a Fe K-edge EXAFS spectra

185 of Si8-FeOx$_{oxid}$ (8 mol% Si relative to Fe) that was similar to that of pure Fh (Fig. 1), with a more

186 developed corner-sharing Fe peak compared to P9-FeOx$_{oxid}$ (Fig. 1B). The PCA-ITFA results

187 indicated that Si8-FeOx$_{oxid}$ consisted of 100% poorly ordered Si-HFO. The ITFA-LCF results are

188 presented in detail in the Supporting Information.

189

190 **Transformation of FeOx in freshwater sediment.** The ITFA results for the entire Fe K-edge

191 EXAFS dataset indicated that all sample spectra, including starting materials, samples from

192 freshwater Site 1 and samples from the sulfidation experiment, could be reproduced by three

193 independent components that represented Fh, Lp and FeS (see Supporting Information).

194   The pore-water in the freshwater drainage ditch was rich in Fe(II) (up to 600 µmol L^{-1}) and P

195 (up to 566 µmol L^{-1}) (Figure 2A). Dissolved sulfide was not detected with the DGT sulfide-binding

196 gel. Due to spectral similarity, all spectra of the hydrogel samples from Site 1 were reproduced in

197 ITFA-LCF by one component — poorly ordered FeOx. To further explore potential minor changes

198 in FeOx structure, we also performed LCF on these samples in Athena[37] using Fh and P9-FeOx$_{hydr}$

199 or Si9-FeOx$_{hydr}$ as references. Preliminary LCF had shown that candidate references such as

200 lepidocrocite, goethite, hematite, magnetite, vivianite, siderite were all negligible. There were also

201 no observable shifts in the Fe-K absorption edge (Fig. 2B), further refuting formation of reduced

202 Fe phases in the hydrogels, even though chemical modelling in Visual Minteq 3.1 (settings: 500

203 µmol L^{-1} Fe(II) and P, pH 6.8, I = 0.01) indicated that the pore-water was oversaturated (saturation

204 index ≈ 8) with respect to vivianite. The LCF results indicated a shift from Si9-FeOx$_{hydr}$ and P9-

205 FeOx$_{hydr}$ to Fh during deployment of the amended FeOx$_{hydr}$ (Fig. 2B), suggesting a minor increase

206 in short-range structure. It is possible that ageing during storage of the FeOx suspensions
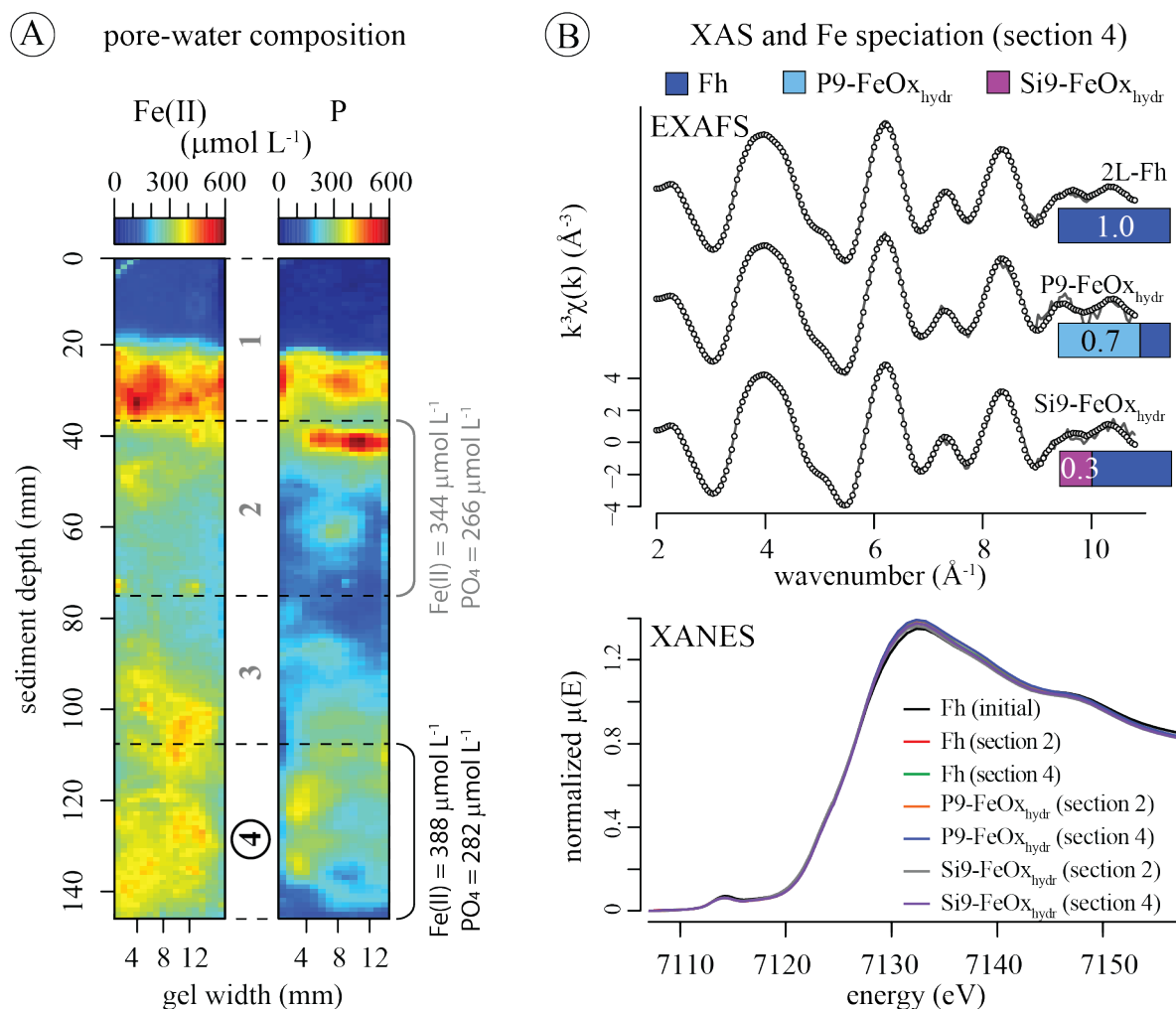
207 contributed to this change.

Figure 2. (A) Pore-water concentrations of Fe(II) and P in the freshwater sediment from Site 1. (B) Upper panel: data (lines) and fits (dots) for bulk Fe K-edge EXAFS spectra for selected FeOx-BT hydrogel sections after deployment (also see Fig. S6 and Table S1). Bar charts show LCF results. Numbers in the bars show fraction of starting FeOx remaining. Lower panel: XANES spectra of initial Fh and Fh, P9-FeOx$_{hydr}$ and Si9-FeOx$_{hydr}$ after deployment.

The limited extent of FeOx crystallization found here contrasts with rapid and extensive Fe(II)-catalyzed transformation of poorly ordered FeOx observed in laboratory studies.[14-15, 40-42] For example, Hansel et al.[15] observed that in sediment columns with advective flow of artificial groundwater with $100 - 300$ μmol L^{-1} Fe(II), 70% of Fh was transformed into Lp and Gt within hours. Transformation will likely be more rapid under advective flow compared to our diffusion-

215   limited experiment with passive samplers in natural sediment, but significant FeOx transformation

216   was expected during a four-week deployment in Fe(II)-rich sediment. Our observations are best

217   explained by the difference in solution chemistry in the sediments relative to aforementioned

218   laboratory studies. The sediments we investigated were characterized by a high dissolved P

219   concentration (> 250 µmol L^{-1}) and are also likely to contain dissolved organic carbon. By binding

220   to FeOx surfaces, P and other strongly-sorbing inorganic and organic species can passivate the

221   particle surface and decrease the rate of FeOx transformation.[4, 6, 43-44] However, we note that

222   adsorbed species (P and organic carbon) were not determined in the current study.

223   Previous work showed that the apparently minor structural changes to Fh by coprecipitation of

224   P or Si notably enhance reductive and acidic dissolution rates (i.e. destabilized the FeOx), likely

225   due to altered macroscopic properties such as decreased particle aggregation.[2, 6] In the current

226   study, FeOx surface passivation by adsorption of P (and potentially other abundant pore-water

227   species) overwhelmed any potential effects on altered FeOx properties from P or Si

228   coprecipitation. Inhibition of FeOx transformation acts to preserve poorly ordered FeOx that have

229   relatively high sorption capacity compared to more crystalline counterparts such as Lp and Gt.

230

231   **In-situ transformation of FeOx in sulfidic tidal flat sediment.** The surface sediment from

232   the tidal flat in the southwest of The Netherlands contained relatively low concentrations (< 20

233   µmol L^{-1}) of dissolved Fe(II) and P compared to the freshwater ditch (see Supporting Information)

234   and showed signs of abundant burrows. During recovery of the samplers, we observed that

235   sediment around the samplers had been eroded to different degrees, resulting in small-scale

236   variability in the sediment depth interval covered by the sampler. Visual inspection of the FeOx-
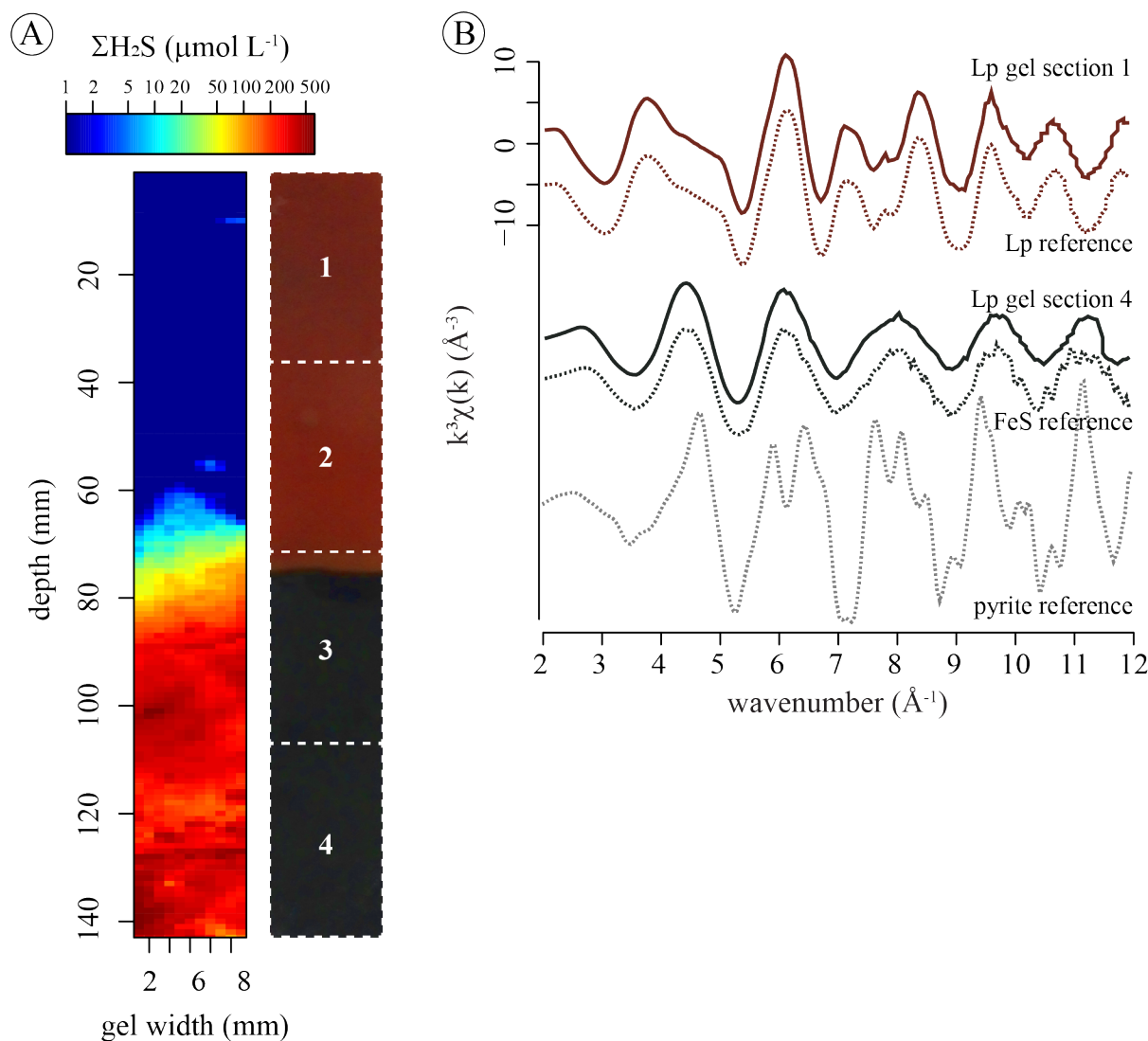
Figure 3. (A) Dissolved ΣH_2S pore-water map determined by DGT hydrogel (left) and image of Lp hydrogel (right) after 4 weeks of deployment in sediment with high dissolved ΣH_2S at depth. Dashed lines and white numbers indicate sections into which the gel was cut for bulk Fe speciation. (B) Fe K-edge EXAFS spectra of Lp gel section 1 and 4 plotted with the Lp, FeS and pyrite (FeS_2) reference spectra.

BT hydrogels after recovery showed strong variability in the depth of the sulfidation front, between 2 to 10 cm sediment depth (see Supporting Information). Visual and spectroscopic evidence of FeOx transformation due to sulfidation was observed in all FeOx-BT hydrogels deployed at Site 2. However, the high spatial variability in chemical conditions in the sediment, likely due to tidal

13

243   effects and bioturbation, did not allow for systematic analysis of the effect of FeOx structure on

244   degree of sulfidation. Therefore, in this section we focus on individual samplers. The sharp

245   transition from anoxic to sulfidic conditions with dissolved ΣH_2S concentrations up to ~ 500 µmol

246   L^{-1} as recorded by DGT sampling (which is an average calculated from integrated sulfide

247   accumulation in the DGT gel over the deployment period[35]) (Fig. 3A, left image) was reflected in

248   a Lp-loaded hydrogel as a sharp color change (Fig. 3A, right image). Synchrotron-based Fe

249   speciation in the top and bottom slices of the Lp hydrogel showed complete transformation of Lp

250   to iron monosulfide (FeS) during deployment in the sulfidic sediment (Fig. 3B). The Fe K-edge

251   XAS results did not show pyrite (FeS_2) formation in the analyzed gel sections from Site 2 after

252   four weeks of deployment. These results highlight the potential for extensive alteration of gel-

253   embedded FeOx. Furthermore, the results are in line with other field studies[39, 45] that show

254   relatively slow transformation of FeS to pyrite under natural sulfidic conditions compared to
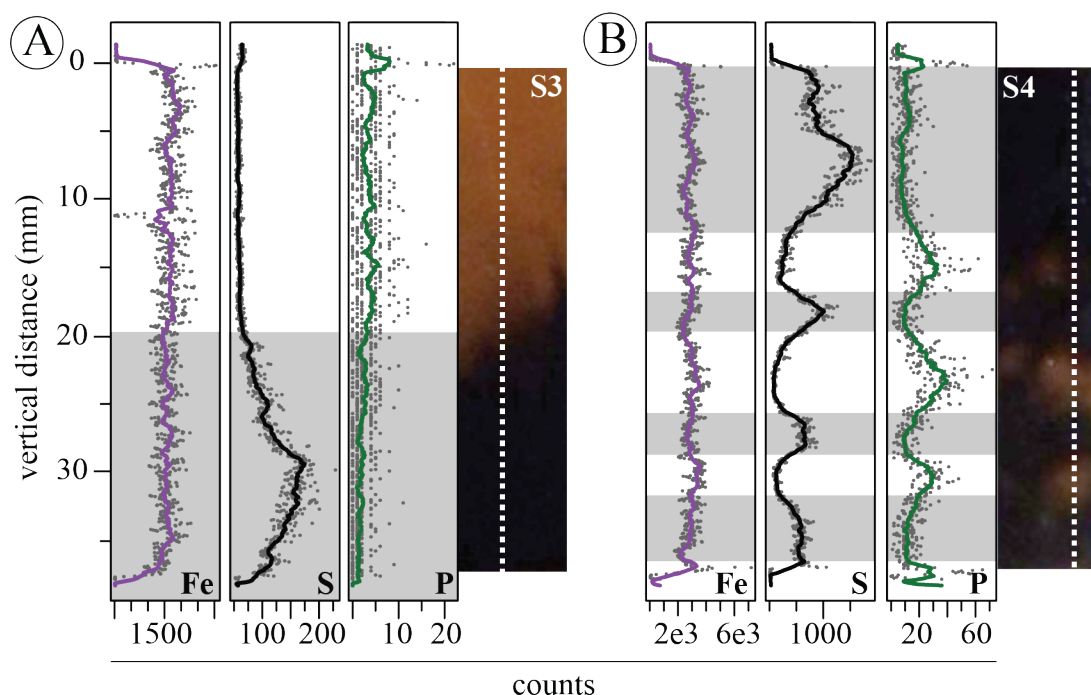
255   laboratory experiments.[46]

Figure 4. Line scans of iron (Fe), sulfur (S) and phosphorus (P) in sections of a P9-FeOx$_{hydr}$ hydrogel deployed under sulfidic field conditions at Site 2. Images of analyzed gel sections to the right, line scan indicated as dashed white line. (A) Scan across the sulfidation front; (B) Scan across patchy region with sulfidized (dark) and non-sulfidized (light) areas.

To investigate the impact of reaction with dissolved sulfide on FeOx transformation and nutrient dynamics, high-resolution element scans were performed with μXRF on a P9-FeOx$_{hydr}$-loaded hydrogel. We selected intervals that captured the sulfidation front (S3, 7–10.5 cm) and a mottled sulfidation pattern (S4, 10.5–14 cm) (Fig. 4). The μXRF line scan across the sulfidation front showed an increase in solid-phase S content and a concurrent decrease in P (Fig. 4A). A line scan across a patchy area in the bottom gel section (with better vacuum and higher counts) showed an even more clear anti-correlation between S and P (Fig. 4B), reflecting release of P by Fe sulfidation.[47] In contrast to S and P, Fe counts were stable throughout the gel sections, irrespective of sulfidation. Similar stable Fe counts were observed across sulfidation fronts in hydrogels with Fh and Si9-FeOx$_{hydr}$ (data not shown). Leaching of Fe from FeOx-BT hydrogels was apparently

15

268   limited during reaction with dissolved $\Sigma H_2 S$, in line with sedimentary evidence for efficient Fe

269   retention under sulfidic conditions.[48]

270

271   **Laboratory-based FeOx sulfidation experiment with natural sediment.** Under stagnant

272   conditions at room temperature (21 °C), dissolved $\Sigma H_2 S$ accumulated with concentrations in

273   excess of 2 mmol L^{-1} within 5 cm sediment depth (SI section S2.6). Dissolved P showed an increase

274   below ~ 1 cm sediment depth and reached concentrations at depth up to ~ 100 µmol L^{-1}. The DET

275   for dissolved Fe(II) was compromised but indicated a similar small peak (< 50 µmol L^{-1}) Fe(II) in

276   the non-sulfidic surface sediment (0–2 cm sediment depth) as was observed in the sediment core

277   (see SI for details). We analyzed Fe speciation in mid-depth, ($\Sigma H_2 S$ 0.8–1.8 mmol L^{-1}) and bottom

278   ($\Sigma H_2 S \geq 2$ mmol L^{-1}) sections of FeOx-BT hydrogels after overnight deployment. The sample

279   spectra and LCF results can be found in SI section S2.7. The results showed that the degree of

280   sulfidation (DOS, here calculated as FeS-Fe/Fe_{tot}) for FeOx from Fe(II) oxidation was consistently

281   higher in bottom sections that were exposed to higher $\Sigma H_2 S$ concentrations (Fig. 5). For FeOx

282   from Fe(III) hydrolysis, such a correlation between DOS and $\Sigma H_2 S$ concentration was not
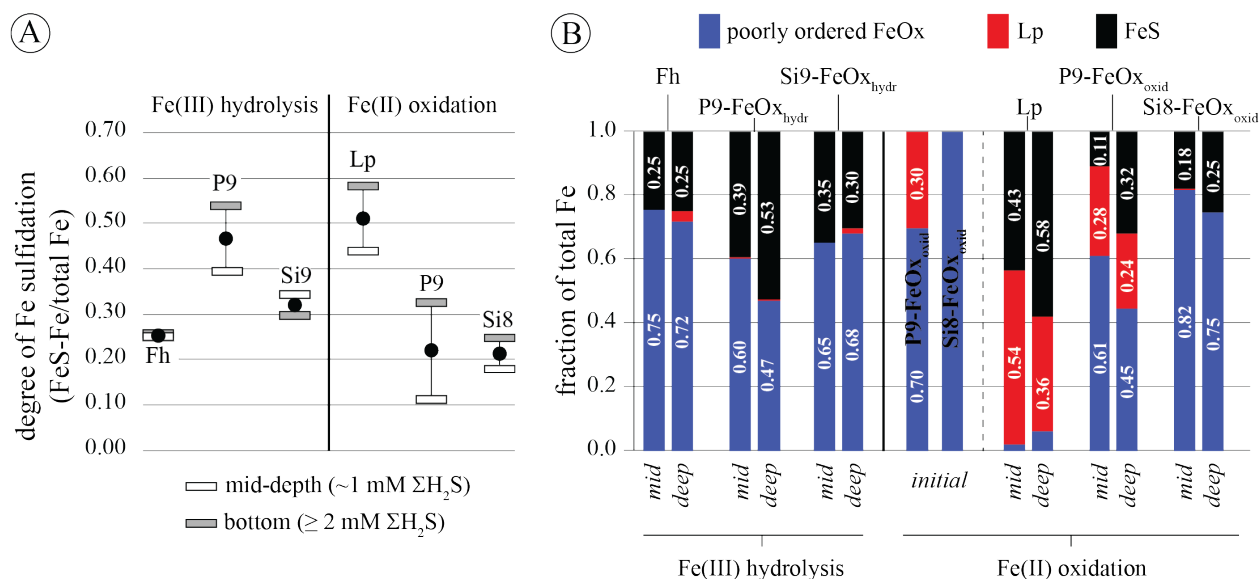
283   observed.

16

284

Figure 5. (A) Degree of Fe sulfidation (i.e. FeS as fraction of total Fe) in FeOx-BT hydrogel sections, grouped by FeOx synthesis method (Fe(III) hydrolysis versus Fe(II) oxidation). White and grey bars represent DOS in mid-depth and bottom hydrogel sections, respectively; black dots indicate the mean DOS value (n = 2). (B) ITFA-LCF results for the FeOx-BT hydrogels sections. For reference, Fe speciation in the P9-FeOx$_{oxid}$ and Si8-FeOx$_{oxid}$ starting materials is shown. *Mid* and *deep* refer to mid-depth (3.5–7 cm) and bottom (10.5–14 cm) sections of the hydrogels, respectively.

285

286 When comparing the pure starting materials Fh and Lp, the DOS was higher for Lp (0.43–0.58)

287 than for Fh (0.25). This may be attributed to relatively rapid ΣH_2S oxidation by Fh, leading to local

288 depletion of ΣH_2S and limited FeS formation. The reactivity of Lp towards sulfide is about an

289 order of magnitude slower compared to Fh[49-50], limiting ΣH_2S depletion in and around the Lp-

290 bearing hydrogel. Furthermore, laboratory studies on FeOx sulfidation pathways suggest that Fh-

291 type FeOx can facilitate relatively rapid surface-to-bulk electron transport compared to more

292 crystalline FeOx such as Lp. As a result, Fe(II) formed at the Fh surface by reaction with dissolved

293 ΣH_2S is re-oxidized to Fe(III) while structural non-sulfidized Fe(II) ("excess Fe(II)") forms, which

294 prevents FeS formation at the Fh surface. This excess Fe(II) has been determined chemically but

295   has so far escaped spectroscopic (Mössbauer) characterization.[18, 51] In our study, ITFA-LCF did

296   not indicate the presence of a Fe(II) phase other than FeS, but the Fe K-edge XANES data may

297   provide some tentative evidence for formation of non-sulfidized Fe(II) (see Supporting

298   Information). Overall, diffusion-limited ΣH_2S supply potentially combined with formation of non-

299   sulfidized excess Fe(II) at the expense of FeS formation may explain the relatively low DOS for

300   poorly ordered Fh compared to Lp.

301   The DOS of P9-FeOx$_{hydr}$ and (to a lesser extent) Si9-FeOx$_{hydr}$ was elevated relative to pure Fh

302   (Fig. 5A). We propose that coprecipitation of P or Si lowers the rate of ΣH_2S oxidation at the Fh

303   surface (at P/Fe = 0.1, approximately half of reactive surface sites on Fh-type FeOx are occupied[6,

304   52]), thereby decreasing diffusion limitations to sulfidation as described above. Surface passivation

305   by P has been suggested to inhibit reaction of dissolved ΣH_2S with FeOx surfaces.[44] Silicate

306   sorption had a more limited effect on DOS than P, likely because Si has a lower affinity for FeOx

307   surfaces.[7, 53-54]

308   Coprecipitation of P or Si during Fe(II) oxidation resulted in a shift in reaction products from

309   Lp to highly disordered HFO (Fig. 1). Consistent with this shift to highly reactive FeOx that deplete

310   dissolved ΣH_2S, the DOS of P9-FeOx$_{oxid}$ and Si8-FeOx$_{oxid}$ markedly decreased (0.1–0.3: Fig. 5B)

311   relative to Lp. For Si8-FeOx$_{oxid}$, the value and small range of DOS were similar to Fh, supporting

312   the XAS results that indicated that Si8-FeOx$_{oxid}$ consisted of Si-HFO with a structure similar to Fh

313   (Fig. 1, Fig. S3). Furthermore, the DOS of Si8-FeOx$_{oxid}$ indicated that occupation of FeOx surface

314   sites by Si did not interfere with sulfidation under the experimental conditions (ΣH_2S 1–2 mmol

315   L^{-1}) and Si/Fe of ~ 0.1. Moreover, the commonalities between Fh and Si8-FeOx$_{oxid}$ suggest that

316   FeOx preparation by Fe(III) hydrolysis produces a poorly ordered FeOx that is representative of

317   natural Fh-like material that commonly forms by Fe(II) oxidation in the presence of dissolved Si.[29]

318   For P9-FeOx$_{oxid}$, a 70:30 mixture of highly disordered P-HFO and Lp (Fig. 1, Fig. S3), the

319   overall DOS showed relatively large variability (Fig. 5B) and differences existed between DOS of

320   the individual Fe components (Fig. 5A). Approximately 5 and 20% of Lp was sulfidized in the

321   mid-depth and bottom sections, respectively, compared to 10 and 40% for P-HFO. This suggests

322   that reaction with highly reactive P-HFO can deplete ΣH_2S and inhibit sulfidation of co-occurring

323   Lp.

324

325   **Implications.** Our experimental approach with gel-based diffusive samplers was able to show

326   that structural alterations in FeOx caused by coprecipitation of oxyanions such as PO$_4$ and SiO$_4$

327   can alter the environmental fate of FeOx. In the case of FeOx sulfidation, poorly ordered, highly

328   reactive FeOx can rapidly deplete dissolved sulfide and thereby limit sulfidation and the associated

329   release of nutrients and contaminants. Diffusion-limited resupply of dissolved sulfide may be more

330   pronounced for gel-embedded FeOx but can also occur in natural sediments when local sulfide

331   gradients develop due to fast reaction of FeOx with sulfide. As such, differences in the rate and

332   extent of sulfidation of FeOx might be particularly relevant in dynamic coastal systems with strong

333   (diurnal) variations in redox conditions. At the same time, environmental conditions, such as high

334   pore-water P concentrations and subsequent FeOx surface passivation, can be the dominating

335   factor controlling FeOx transformations and overwhelm the effect of structural differences.

336   Furthermore, our results show different behavior of amended FeOx from Fe(III) hydrolysis and

337   Fe(II) oxidation, suggesting that laboratory-based findings from Fe(III)-derived Fh-type

338   precipitates may not always be transferable to natural settings, where poorly ordered FeOx

339   commonly form by Fe(II) oxidation. We show that deploying FeOx in natural sediments using gel-

340   based diffusive samplers can elucidate the processes controlling environmental FeOx cycling

341   under natural conditions and help bridge the gap between laboratory experiments and the

342   environmental fate of FeOx.

ASSOCIATED CONTENT

Supporting Information Available.

Detailed descriptions of FeOx synthesis; Preparation of hydrogels and samplers; Deployment and recovery of samplers; Analysis of DGT and DET gels; Sample preparation and analysis for micro-scale XRF and XAS; PCA-ITFA results for entire dataset; ITFA-LCF results for P9-FeOx$_{oxid}$ and Si8-FeOx$_{oxid}$; Fe K-edge spectra and LCF results for FeOx deployed in freshwater Site 1; Pore-water sulfide and phosphate for marine sediment in the laboratory microcosm experiment; Results of ITFA analysis of the Fe K-edge EXAFS spectra for samples from the laboratory sulfidation experiment; XANES results from the laboratory sulfidation experiment. This material is available free of charge via the Internet at http://pubs.acs.org.

AUTHOR INFORMATION

Corresponding Author

* Phone: +31-222-369455

Author Contributions

The manuscript was written through contributions of all authors. All authors have given approval to the final version of the manuscript.

ABBREVIATIONS

DET, diffusive equilibrium in thin films; DGT, diffusive gradients in thin films; EXAFS, extended X-ray fine structure; FeOx-BT, FeOx-bearing thin film; Fh, (2-line) ferrihydrite; Lp, lepidocrocite; Mag, magnetite; XANES, X-ray Absorption Near-Edge Spectroscopy; XAS, X-ray absorption spectroscopy

REFERENCES

1.   van Genuchten, C. M.; Gadgil, A. J.; Peña, J. Fe(III) Nucleation in the Presence of Bivalent Cations and Oxyanions Leads to Subnanoscale 7 Å Polymers. *Environ. Sci. Technol.* **2014,** *48* (20), 11828-11836.
2.   Kaegi, R.; Voegelin, A.; Folini, D.; Hug, S. J. Effect of phosphate, silicate, and Ca on the morphology, structure and elemental composition of Fe(III)-precipitates formed in aerated Fe(II) and As(III) containing water. *Geochim. Cosmochim. Acta* **2010,** *74* (20), 5798-5816.

3.   Voegelin, A.; Kaegi, R.; Frommer, J.; Vantelon, D.; Hug, S. J. Effect of phosphate, silicate, and Ca on Fe(III)-precipitates formed in aerated Fe(II)- and As(III)-containing water studied by X-ray absorption spectroscopy. *Geochim. Cosmochim. Acta* **2010,** *74* (1), 164-186.

4.   Paige, C. R.; Snodgrass, W. J.; Nicholson, R. V.; Scharer, J. M.; He, Q. H. The effect of phosphate on the transformation of ferrihydrite into crystalline products in alkaline media. *Water, Air, & Soil Pollution* **1997,** *97* (3), 397-412.

5.   Cornell, R. M.; Giovanoli, R.; Schindler, P. W. Effect of silicate species on the transformation of ferrihydrite into goethite and hematite in alkaline media. *Clays & Clay Minerals* **1987,** *35* (1), 21-28.

6.   Kraal, P.; van Genuchten, C. M.; Behrends, T.; Rose, A. L. Sorption of phosphate and silicate alters dissolution kinetics of poorly crystalline iron (oxyhydr)oxide. *Chemosphere* **2019,** *234*, 690-701.

7.   van Genuchten, C. M.; Peña, J.; Amrose, S. E.; Gadgil, A. J. Structure of Fe(III) precipitates generated by the electrolytic dissolution of Fe(0) in the presence of groundwater ions. *Geochim. Cosmochim. Acta* **2014,** *127*, 285-304.

8.   Voegelin, A.; Senn, A.-C.; Kaegi, R.; Hug, S. J.; Mangold, S. Dynamic Fe-precipitate formation induced by Fe(II) oxidation in aerated phosphate-containing water. *Geochim. Cosmochim. Acta* **2013,** *117*, 216-231.

9.   Waychunas, G. A.; Rea, B. A.; Fuller, C. C.; Davis, J. A. Surface chemistry of ferrihydrite: Part 1. EXAFS studies of the geometry of coprecipitated and adsorbed arsenate. *Geochim. Cosmochim. Acta* **1993,** *57* (10), 2251-2269.

10.   Rose, J.; Manceau, A.; Bottero, J.-Y.; Masion, A.; Garcia, F. Nucleation and growth mechanisms of Fe oxyhydroxide in the presence of PO_4 ions. 1. Fe K-Edge EXAFS study. *Langmuir* **1996,** *12* (26), 6701-6707.

11.   Rozan, T. F.; Taillefert, M.; Trouwborst, R. E.; Glazer, B. T.; Ma, S.; Herszage, J.; Valdes, L. M.; Price, K. S.; Iii, G. W. L. Iron-sulfur-phosphorus cycling in the sediments of a shallow coastal bay: Implications for sediment nutrient release and benthic macroalgal blooms. *Limnol. Oceanogr.* **2002,** *47* (5), 1346-1354.

12.   Krom, M. D.; Berner, R. A. Adsorption of phosphate in anoxic marine sediments. *Limnol. Oceanogr.* **1980,** *25* (5), 797-806.

13.   Cornell, R. M.; Schwertmann, U., *The Iron Oxides: Structure, Properties, Reactions, Occurrences and Uses*. Wiley: 2003; p 664.

14.   Hansel, C. M.; Benner, S. G.; Fendorf, S. Competing Fe(II)-induced mineralization pathways of ferrihydrite. *Environ. Sci. Technol.* **2005,** *39* (18), 7147-7153.

15.   Hansel, C. M.; Benner, S. G.; Neiss, J.; Dohnalkova, A.; Kukkadapu, R. K.; Fendorf, S. Secondary mineralization pathways induced by dissimilatory iron reduction of ferrihydrite under advective flow. *Geochim. Cosmochim. Acta* **2003,** *67* (16), 2977-2992.

16.   Burton, E. D.; Johnston, S. G.; Bush, R. T. Microbial sulfidogenesis in ferrihydrite-rich environments: Effects on iron mineralogy and arsenic mobility. *Geochim. Cosmochim. Acta* **2011,** *75* (11), 3072-3087.

17.   Yang, L.; Steefel, C. I.; Marcus, M. A.; Bargar, J. R. Kinetics of Fe(II)-Catalyzed Transformation of 6-line Ferrihydrite under Anaerobic Flow Conditions. *Environ. Sci. Technol.* **2010,** *44* (14), 5469-5475.

18. Peiffer, S.; Behrends, T.; Hellige, K.; Larese-Casanova, P.; Wan, M.; Pollok, K. Pyrite formation and mineral transformation pathways upon sulfidation of ferric hydroxides depend on mineral type and sulfide concentration. *Chem. Geol.* **2015**, *400*, 44-55.

19. Davison, W.; Zhang, H. In situ speciation measurements of trace components in natural waters using thin-film gels. *Nature* **1994**, *367* (6463), 546-548.

20. Davison, W.; Grime, G. W.; Morgan, J. A. W.; Clarke, K. Distribution of dissolved iron in sediment pore waters at submillimetre resolution. *Nature* **1991**, *352* (6333), 323-325.

21. Michel, F. M.; Ehm, L.; Antao, S. M.; Lee, P. L.; Chupas, P. J.; Liu, G.; Strongin, D. R.; Schoonen, M. A. A.; Phillips, B. L.; Parise, J. B. The structure of ferrihydrite, a nanocrystalline material. *Science* **2007**, *316* (5832), 1726-1729.

22. Hiemstra, T. Surface and mineral structure of ferrihydrite. *Geochim. Cosmochim. Acta* **2013**, *105* (0), 316-325.

23. Schwertmann, U.; Cornell, S., *Iron oxides in the laboratory: Preparation and characterization*. Wiley: 1991; p 188.

24. Bigham, J. M.; Schwertmann, U.; Traina, S. J.; Winland, R. L.; Wolf, M. Schwertmannite and the chemical modeling of iron in acid sulfate waters. *Geochim. Cosmochim. Acta* **1996**, *60* (12), 2111-2121.

25. Ferris, F. G.; Tazaki, K.; Fyfe, W. S. Iron oxides in acid mine drainage environments and their association with bacteria. *Chem. Geol.* **1989**, *74* (3), 321-330.

26. Yu, J.-Y.; Heo, B.; Choi, I.-K.; Cho, J.-P.; Chang, H.-W. Apparent solubilities of schwertmannite and ferrihydrite in natural stream waters polluted by mine drainage. *Geochim. Cosmochim. Acta* **1999**, *63* (19), 3407-3416.

27. Carlson, L.; Bigham, J. M.; Schwertmann, U.; Kyek, A.; Wagner, F. Scavenging of As from Acid Mine Drainage by Schwertmannite and Ferrihydrite: A Comparison with Synthetic Analogues. *Environ. Sci. Technol.* **2002**, *36* (8), 1712-1719.

28. Jambor, J. L.; Dutrizac, J. E. Occurrence and constitution of natural and synthetic ferrihydrite, a widespread iron oxyhydroxide. *Chemical Reviews* **1998**, *98* (7), 2549-2586.

29. Schwertmann, U., Occurrence and Formation of Iron Oxides in Various Pedoenvironments. In *Iron in Soils and Clay Minerals*, Stucki, J. W.; Goodman, B. A.; Schwertmann, U., Eds. Springer Netherlands: Dordrecht, 1988; pp 267-308.

30. Jensen, H. S.; Kristensen, P.; Jeppesen, E.; Skytthe, A. Iron-phosphorus ratio in surface sediment as an indicator of phosphate release from aerobic sediments in shallow lakes. *Hydrobiologia* **1992**, *235*, 731-743.

31. Kraal, P.; Dijkstra, N.; Behrends, T.; Slomp, C. P. Phosphorus burial in sediments of the sulfidic deep Black Sea: key roles for adsorption by calcium carbonate and apatite authigenesis. *Geochim. Cosmochim. Acta* **2017**, *204*, 140-158.

32. Hyacinthe, C.; Van Cappellen, P. An authigenic iron phosphate phase in estuarine sediments: composition, formation and chemical reactivity. *Mar. Chem.* **2004**, *91* (1-4), 227-251.

33. Bennett, W. W.; Teasdale, P. R.; Welsh, D. T.; Panther, J. G.; Jolley, D. F. Optimization of colorimetric DET technique for the in situ, two-dimensional measurement of iron(II) distributions in sediment porewaters. *Talanta* **2012**, *88* (0), 490-495.

34. Pagès, A.; Teasdale, P. R.; Robertson, D.; Bennett, W. W.; Schäfer, J.; Welsh, D. T. Representative measurement of two-dimensional reactive phosphate distributions and co-distributed iron(II) and sulfide in seagrass sediment porewaters. *Chemosphere* **2011**, *85* (8), 1256-1261.

35.   Robertson, D.; Teasdale, P. R.; Welsh, D. T. A novel gel-based technique for the high resolution, two-dimensional determination of iron (II) and sulfide in sediment. *Limnol. Oceanogr. Meth.* **2008,** *6*, 502-512.

36.   Nikitenko, S.; Beale, A. M.; van der Eerden, A. M. J.; Jacques, S. D. M.; Leynaud, O.; O'Brien, M. G.; Detollenaere, D.; Kaptein, R.; Weckhuysen, B. M.; Bras, W. Implementation of a combined SAXS/WAXS/QEXAFS set-up for time-resolved in situ experiments. *J. Synchrotron Radiat.* **2008,** *15* (6), 632-640.

37.   Ravel, B.; Newville, M. Athena, Artemis, Hephaestus: data analysis for X-ray absorption spectroscopy using IFEFFIT. *J. Synchrotron Radiat.* **2005,** *12*, 537-541.

38.   Rossberg, A.; Reich, T.; Bernhard, G. Complexation of uranium(VI) with protocatechuic acid—application of iterative transformation factor analysis to EXAFS spectroscopy. *Anal. Bioanal. Chem.* **2003,** *376* (5), 631-638.

39.   Boesen, C.; Postma, D. Pyrite formation in anoxic environments of the Baltic. *Am. J. Sci.* **1988,** *288* (6), 575-603.

40.   Jones, A. M.; Collins, R. N.; Waite, T. D. Redox characterization of the Fe(II)-catalyzed transformation of ferrihydrite to goethite. *Geochim. Cosmochim. Acta* **2017,** *218*, 257-272.

41.   Pedersen, H. D.; Postma, D.; Jakobsen, R.; Larsen, O. Fast transformation of iron oxyhydroxides by the catalytic action of aqueous Fe(II). *Geochim. Cosmochim. Acta* **2005,** *69* (16), 3967-3977.

42.   Yee, N.; Shaw, S.; Benning, L. G.; Nguyen, T. H. The rate of ferrihydrite transformation to goethite via the Fe(II) pathway. *Am. Mineral.* **2006,** *91* (1), 92-96.

43.   Schoepfer, V. A.; Burton, E. D.; Johnston, S. G.; Kraal, P. Phosphate loading alters schwertmannite transformation rates and pathways during microbial reduction. *Sci. Total Environ.* **2019,** *657*, 770-780.

44.   Biber, M. V.; dos Santos Afonso, M.; Stumm, W. The coordination chemistry of weathering: IV. Inhibition of the dissolution of oxide minerals. *Geochim. Cosmochim. Acta* **1994,** *58* (9), 1999-2010.

45.   Kraal, P.; Burton, E. D.; Bush, R. T. Iron monosulfide accumulation and pyrite formation in eutrophic estuarine sediments. *Geochim. Cosmochim. Acta* **2013,** *122* (0), 75-88.

46.   Rickard, D. Kinetics of pyrite formation by the H_2S oxidation of iron (II) monosulfide in aqueous solutions between 25 and 125°C: The rate equation. *Geochim. Cosmochim. Acta* **1997,** *61* (1), 115-134.

47.   Slomp, C. P.; Van Raaphorst, W. Phosphate adsorption in oxidized marine sediments. *Chem. Geol.* **1993,** *107* (3-4), 477-480.

48.   Scholz, F.; McManus, J.; Mix, A. C.; Hensen, C.; Schneider, R. R. The impact of ocean deoxygenation on iron release from continental margin sediments. *Nature Geosci.* **2014,** *7* (6), 433-437.

49.   Poulton, S. W.; Krom, M. D.; Raiswell, R. A revised scheme for the reactivity of iron (oxyhydr)oxide minerals towards dissolved sulfide. *Geochim. Cosmochim. Acta* **2004,** *68* (18), 3703-3715.

50.   Canfield, D. E.; Raiswell, R.; Bottrell, S. H. The reactivity of sedimentary iron minerals toward sulfide. *Am. J. Sci.* **1992,** *292* (9), 659-683.

51.   Hellige, K.; Pollok, K.; Larese-Casanova, P.; Behrends, T.; Peiffer, S. Pathways of ferrous iron mineral formation upon sulfidation of lepidocrocite surfaces. *Geochim. Cosmochim. Acta* **2012,** *81*, 69-81.

52.   Dzombak, D. A.; Morel, F. M. M., *Surface complexation modeling: Hydrous ferric oxide*. Wiley: New York, 1990; p 416.

53.   Xu, N.; Christodoulatos, C.; Braida, W. Modeling the competitive effect of phosphate, sulfate, silicate, and tungstate anions on the adsorption of molybdate onto goethite. *Chemosphere* **2006,** *64* (8), 1325-1333.

54.   Hiemstra, T. Ferrihydrite interaction with silicate and competing oxyanions: Geometry and Hydrogen bonding of surface species. *Geochim. Cosmochim. Acta* **2018,** *238*, 453-476.

Supporting Information

Coprecipitation of phosphate and silicate affects environmental iron

(oxyhydr)oxide transformations: a gel-based diffusive sampler approach

Peter Kraal, Case M. van Genuchten, Wytze K. Lenstra, Thilo Behrends

15 pages

11 figures

2 tables

1	**Synthesis of FeOx.** Pure two-line ferrihydrite (Fh; $Fe_{10}O_{14}(OH)_2 \cdot nH_2O$ with n < 1)[1-2] was
2	synthesized by rapid base hydrolysis of a concentrated $Fe(III)(NO_3)_3$ solution with CO_2-free
3	(boiled and N_2-purged) 1 M NaOH, following the protocol of Schwertmann and Cornell.[3]
4	Lepidocrocite (Lp; γ-FeOOH) was synthesized by oxidation of a concentrated $Fe(II)Cl_2$
5	solution by bubbling with regular air using a diffuser connected to a compressed air outlet,
6	setting the flow rate to ~ 100 mL min^{-1}.[3] Fh and Lp synthesis was also performed in the
7	presence of dissolved phosphate (PO_4 as $Na_2HPO_4 \cdot 7H_2O$) or silicate (SiO_4 as $Na_2SiO_3 \cdot 9H_2O$)
8	with a molar (P, Si)/Fe ratios of 1/10. These amended protocols, detailed elsewhere,[4] were
9	applied to synthesize ferric iron precipitates (iron (oxyhydr)oxides, referred to here as FeOx)
10	with co-precipitated P or Si. For Fe(III) hydrolysis with coprecipitated P or Si, the NaOH
11	solution was amended with ~ 30 mmol L^{-1} P or Si and added at a rate of ~ 20 mL min^{-1} with a
12	total volume that resulted in a final molar (P, Si)/Fe ratio of 0.1. For FeOx by oxidation of
13	$Fe(II)Cl_2$, a 1 M NaOH solution amended with ~ 50 mmol L^{-1} P or Si was added continuously
14	during oxidation of the Fe(II) solution using a Metrohm Titrando 809 device to buffer pH at
15	6.8, also resulting in a final (P, Si)/Fe ratio of 0.1. Because of the high pH of the Si-amended
16	NaOH stock solution and relatively low Si/Fe ratio during synthesis, it is unlikely that
17	significant Si polymerization occurred in solution or at the FeOx surface.[5-6] Each FeOx
18	precipitate was poured into Spectra/Por 4 regenerated cellulose dialysis tubing
19	(SpectrumLabs) and dialyzed in 10 L of ultrapure water with regular water changes until the
20	electric conductivity was < 10 µS cm^{-1} (4 days). The FeOx were stored in suspension in the
21	dark at 4 °C for up to two weeks prior to further processing. The final concentration in all
22	suspensions was 25 – 30 mg FeOx mL^{-1}. The composition of the FeOx was determined by
23	dissolution of freeze-dried sub-samples in 6 mol L^{-1} HCl and spectrophotometric
24	measurement of Fe, P and Si.
25	
26	**Preparation of (FeOx-BT) hydrogels and samplers.** The preparation of diffusive and
27	binding hydrogels is described in detail in previous studies.[7-9] For this study, FeOx-bearing
28	thin film (FeOx-BT) hydrogels were prepared by mixing adding 3 mL FeOx suspension per
29	10 mL of acrylamide solution, stirring vigorously and adding ammonium persulfate and
30	N,N,N′,N′-tetramethylethylenediamine. This suspension was used to cast 0.8 mm-thick Fe-
31	MDT hydrogels. The total Fe content in the fresh hydrated gels was ~ 60 µmol cm^{-3}, which is
32	in the range of FeOx-Fe contents in oxic surface sediments. Adding FeOx suspension rather
33	than dried FeOx optimized the homogeneity of FeOx distribution after casting the gel. In
34	previous work[10-11], Fh was precipitated directly within the pores of hydrogels. Here, for
35	consistency we preferred to produce stock FeOx suspensions that were used for a range of
36	laboratory and field experiments (also reported elsewhere[4]), including deployment of FeOx-
37	BT hydrogels for the current study. All hydrogels were cleaned with repeated milli-Q baths
38	(at least 5 water changes) and cut into 2.5 × 16 cm hydrogel strips.
39	For pore-water sampling, DGT-DET samplers were prepared by placing a DGT hydrogel strip
40	in a rigid Teflon^{TM} sampler (DGT Research), which was then overlain by a DET hydrogel
41	strip and a strip of 0.45 µm nitrocellulose filter membrane. The gels and filter were kept in
42	place by front window (Fig. S1). For FeOx deployment, instead of a DGT-DET gel stack, a
43	FeOx-BT hydrogel strip was covered by filter membrane.
44	

45

46
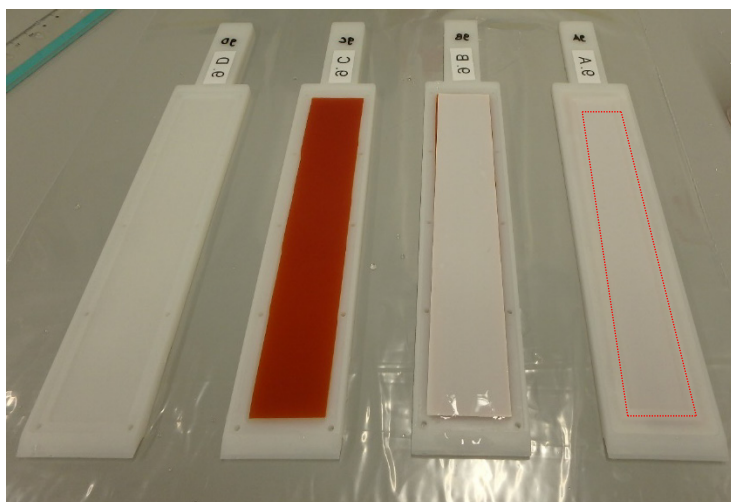
Fig. S1. Preparation of FeOx-BT hydrogel sampler in four steps. From left to right: empty
Teflon sampler (DGT Research); loading of FeOx-BT hydrogel; filter membrane cover;
securing FeOx-BT gel and filter in place with front window (~ 1.5 × 12 cm open area for
diffusive exchaneg, indicated by red dashed line) for solute exchange between gel and pore-
water.

Deployment and recovery of hydrogel samplers. DGT-DET and FeOx-BT samplers
were pushed vertically into the sediment, for pore-water samplers ~ 1 cm of the sampling
window remaining above the sediment-water interface. Pore-water DGT-DET samplers for
Fe(II), P and ΣH_2S were deployed overnight at the beginning of the FeOx deployment period.
The selected FeOx-BT samplers were deployed in the field for four weeks, in duplicate (i.e.
two samplers for each FeOx). At Site 1, samplers were placed in the ditch sediment under ~
50 cm of water. At Site 2, samplers were placed in tidal flat sediment under shallow water (~
20 cm) during low tide, assuming the area never fell completely dry (which would cause the
gels to dry out). Upon recovery, the DGT-DET samplers were processed and analyzed on-site.
The FeOx-BT samplers were placed in ~ 5 L of Ar-purged anoxic water (milliQ for
freshwater Site 1, 0.7 M sodium chloride for marine Site 2) and immediately transported to an
Ar-filled anoxic glovebox in the Utrecht University laboratory, within 4 h after retrieval.
Pore-water sampling with DGT-DET proved challenging at Site 2 because of the low pore-
water Fe(II) and P concentrations. Therefore, we also took a 20 cm-long sediment core with
overlying water that was sectioned at 1-cm vertical resolution in a N_2-purged glovebag within
2 h after recovery. The 1-cm sediment slices were transferred into polyethylene centrifuge
tubes, centrifuged (4000 rpm, 15 min) and the 0.45 µm-filtered supernatant was used for
analysis of dissolved Fe(II), ΣH_2S, P and Si using standard spectrophotometric methods:
molybdate blue (P, Si), methylene blue (ΣH_2S) and 1,10-phenanthroline.[12] The results of this
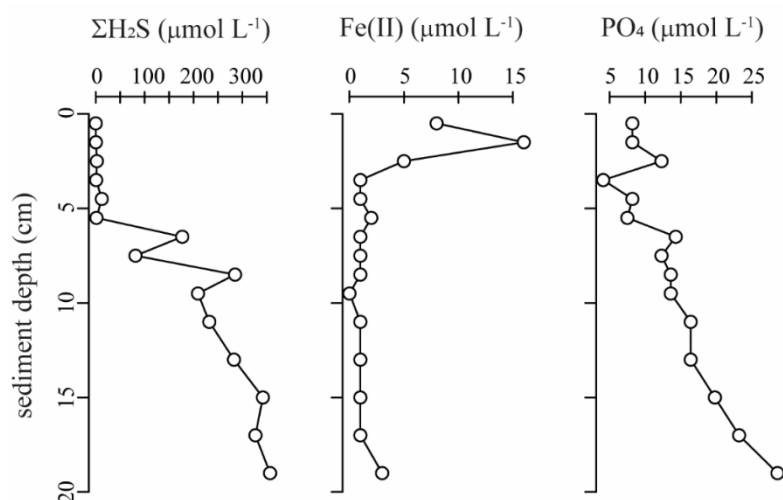classical pore-water sampling are shown in Fig. S2.

76

Fig. S2. Concentration profiles for dissolved ΣH_2S, Fe(II) and P determined by spectrophotometric analysis of filtered pore-water from Site 2.

Upon recovery, inspection of the FeOx-BT hydrogels after deployment at Site 2 showed that there were large differences in the depth of the sulfidation front (S3):
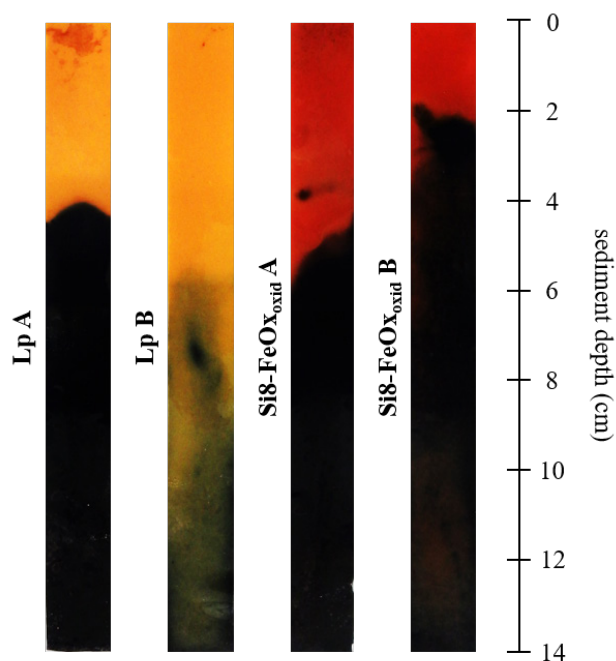

Fig. S3. Images of duplicate Lp and Si8-FeOx$_{oxid}$ gels, showing the large variability in the depth and intensity of the sulfidation front. Image color corrections: saturation (+ 40 %) and contrast (+ 40 %) were increased to enhance visibility of sulfidized gel sections.

Processing and analysis of DGT and DET gels. Duplicate DGT-DET samplers were used for simultaneous Fe(II), P and ΣH_2S measurement. The DET hydrogel from the first probe (sample gel) was removed and immediately covered by a DET hydrogel that had equilibrated (2 h) with a Ferrozine™ solution (staining gel). Upon diffusive exchange, the Ferrozine™ in the staining gel forms a magenta complex with Fe(II) in the sample gel.[13] A similar process was applied to the DET sample gel from the second probe to measure P using a DET staining gel equilibrated in a solution with molybdate and ascorbic acid which forms a reduced blue complex with P.[9] After 15 min, 300 dpi color images of the gel stacks were collected (Canon CanoScan LiDE 210). The color images were converted to monochrome grayscale and the grayscale intensity (GSI) maps were converted into two-dimensional Fe(II) and P distributions, using Fe(II) and P versus GSI calibration curves with a range of 0–1500 and 0–750 $\mu mol\ L^{-1}$ (see below). In the time frame between recovering DGT-DET gels and scanning, diffusional relaxation is limited and fidelity to the sampled distribution of the pore-water Fe(II) and P is retained as much as possible.[7]

The two dissolved sulfide DGT gels from the duplicate DGT-DET samplers were placed overnight in 0.01 mol L^{-1} hydroxylamine to remove staining by FeOx. The gels were then scanned as described for the DET gels. In case of DGT gels, sulfide is bound by reaction with AgI that is mixed into the DGT hydrogel. This reaction results in a color change from yellowish white (AgI hydrogel) to black (Ag_2S stains). Sulfide concentrations were calculated from grayscale intensity using a previously published calibration.[7]

For calibration of the DET method for Fe(II) and P, duplicate series of calibration solutions were prepared. For each analyte, one set of duplicate calibration solutions was prepared in 0.01 M NaCl as freshwater representative and another set of duplicates was prepared in 0.7 M NaCl as seawater representative. For Fe(II), following Bennet et al.[13], a set of ten calibration solutions was prepared using ammonium Fe(II) sulfate covering a 0 - 1500 $\mu mol\ L^{-1}$ Fe(II) range in 0.01 mol L^{-1} hydroxylamine hydrochloride. For P, following Pagès et al.[14], a set of ten calibration solutions was prepared using sodium dihydrogen phosphate covering a 0 - 750 $\mu mol\ L^{-1}$ P range in 5% (v/v) hydrochloric acid. Two circular pieces (1.5 cm diameter) of DET hydrogel were placed in each solution and allowed to equilibrate for at least two hours. At the same time, corresponding gel pieces were placed for at least two hours in the Fe(II) staining reagent (0.01 mol L^{-1} Ferrozine in 0.1 mol L^{-1} acetic acid/sodium acetate) or the P staining reagent (0.045 mol L^{-1} ammonium heptamolybdate, 0.5 mmol L^{-1} potassium antimonyl tartrate, 2.5 mol L^{-1} sulfuric acid, 0.03 mol L^{-1} ascorbic acid). Subsequently, a gel piece from a Fe(II) or P calibration solution was overlain with a gel piece from the appropriate staining reagent. The gel stacks were scanned after 15 minutes and the color intensity was converted to grey scale intensity. The results showed that the upper detection limit was ~ 1000 $\mu mol\ L^{-1}$ for Fe(II) and > 750 $\mu mol\ L^{-1}$ for P (Fig. S4). The practical lower detection limit for both analytes was ~ 10 $\mu mol\ L^{-1}$.[13] As established previously[13], the effect of ionic strength was minor (< 10% difference between 0.01 M NaCl and 0.1 M NaCl) and we only report the results from the 0.7 M NaCl calibration solutions.
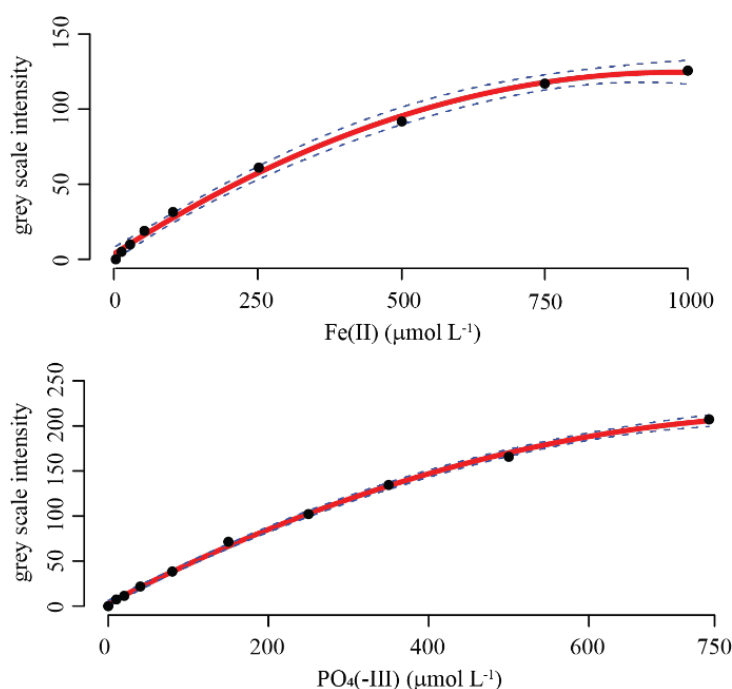
127

Fig. S4. Calibration curves for dissolved Fe(II) (top) and PO_4^{3-} (bottom) in 0.7 M NaCl, showing grey scale intensity plotted against analyte concentration. Black dots show data points, red line is non-linear regression and blue dashed lines represent the 95% confidence interval based on duplicate series.

132

Sample preparation and analysis for micro-scale XRF and synchrotron based XAS. For μXRF analysis, selected gel cuts were placed on an acid-washed glass microscope slide and tightly covered with cling film. The slide with gel cut was then immediately placed in the sample chamber of an Orbis Micro X-ray Fluorescence Analyzer (EDAX) and brought under vacuum. The Orbis EDAX was operated at 30 keV with 30×30 μm spatial resolution and a dwell time of 800 ms. After reaching sufficient vacuum, vertical (one-dimensional) line scans from the top to the bottom of hydrogel sections (~ 3.5 cm) were collected. Because the hydrogel sections dried out under vacuum and started deforming after about 30 min, these analyses were carried out within 20 min of placing gel sections in the vacuum chamber of the Orbis EDAX.

The hydrogel sections for synchrotron-based X-ray absorption spectroscopy (XAS) were freeze-dried under an N_2 atmosphere and powdered in the anoxic glovebox with an agate mortar and pestle. An amount of Fe-doped hydrogel containing the Fe equivalent of ~ 1 absorption length[15] was mixed with microcrystalline cellulose (Sigma-Aldrich) and pressed into a 7 mm-diameter pellet (thickness ~ 1 mm) with a hand press (Pike Technologies). The pellets were transported in Ar-purged, gas-tight aluminum laminate bags to the European Synchrotron Radiation Facility (ESRF) in Grenoble, France. Iron K-edge XAS spectra were collected at beamline BM26A (DUBBLE). Details on the beamline setup can be found in Nikitenko et al.[16] Samples were loaded into the sample holder in an anoxic N_2-purged glovebag at the beamline and data was collected as described in detail previously.[4] In short, samples were sealed between two layers of Kapton tape and spectra were recorded at room

154   temperature in transmission mode from 6962 to 7862 eV, corresponding to a maximum k of
155   13 Å^{-1} in the EXAFS region. For each sample, two spectra were collected and merged.
156   Repeated measurement of FeS-rich samples showed no sign of oxidation or beam damage
157   during analysis. Data normalization and manipulation were performed using the Athena
158   software package.[17] Fourier transformation was performed using a Rkbg value of 1.0, a k-
159   range of 2–11 Å^{-1} and a Hanning window function. Using the ITFA software package[18],
160   principal components analysis (PCA) was performed to assess the required number
161   independent components to reproduce the major variance of the entire EXAFS data set that
162   consisted of 24 spectra: FeOx starting materials, samples from the freshwater Site 1 hydrogels
163   and hydrogel samples from the laboratory-based sulfidation experiment. Also included was an
164   existing reference spectrum of synthetic mackinawite (FeS).[19] The components were extracted
165   from the dataset by iterative transformation factor analysis (ITFA), and linear combination
166   fitting (LCF) was used to determine the relative contribution of the independent components
167   to each sample spectrum (i.e. Fe speciation). PCA-ITFA-LCF analysis was performed in k
168   space, using a fitting window of $k = 2$ - 11 Å^{-1} of the k^3 weighted EXAFS spectra. The ITFA
169   analysis requires that the relative concentration of each independent component is constrained
170   in at least one sample. The starting materials Fh and Lp and the reference spectrum of FeS
171   were used as endmembers: the relative concentration of the component with the strongest
172   loading was set to 1 and that of all other components to 0.

173

174   **PCA-ITFA analysis of the Fe K-edge EXAFS dataset.** Principal component analysis
175   (PCA) and iterative transformation factor analysis (ITFA) on all normalized EXAFS spectra
176   (FeOx starting materials, freshwater samples, samples from laboratory-based sulfidation
177   experiment) were performed with the ITFA software.[18] PCA showed that the major variance
178   in the EXAFS dataset could be reproduced using three components (Fig. S5).
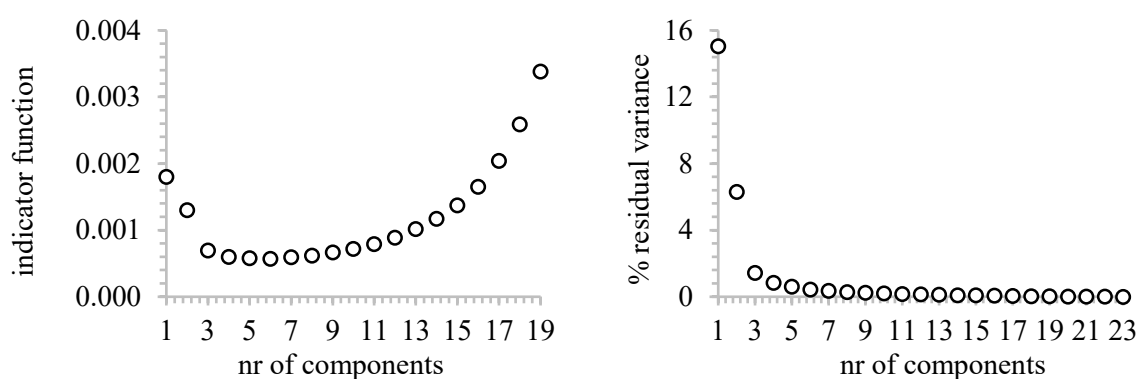
179

180

181   **Fig. S5**. ITFA indicator function plotted against number of independent components (left) and
182   % residual variance as function of number of components (right). Minimum error and low
183   residual variance indicate that optimal results are obtained with using three components to
184   reproduce the sample spectra. Note: the indicator function rapidly increased for number of
185   components > 19 and therefore errors using 20–23 components are omitted in the left panel as
186   it would mask the decrease in error for low numbers of components.

187 The components showed spectral properties similar to the spectra of the Fe reference
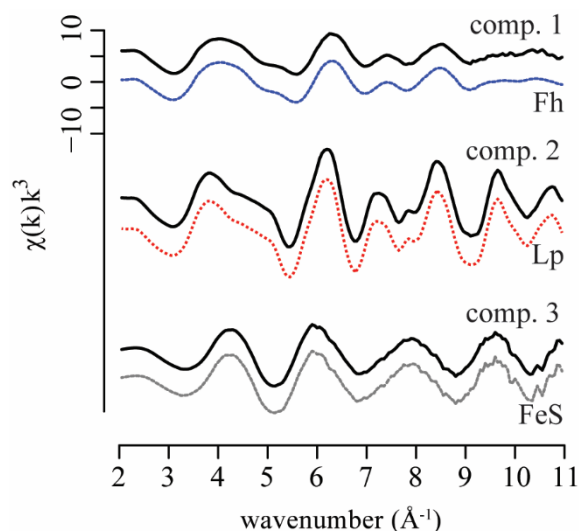188 standards Fh, Lp and FeS (Fig. S6).

189

190 **Fig. S6**. Spectra of the three ITFA components and the three reference materials (Fh, Lp and
191 FeS) that these components represent.

192

193 **Fe speciation from PCA-ITFA in starting materials from Fe(II) oxidation**. Linear
194 combination fitting (LCF) using the spectra of the PCA-ITFA-derived independent
195 components indicated that P9-FeOx$_{oxid}$ was a mixture of highly disordered P-HFO (70 %) and
196 Lp (30 %). The spectrum of Si8-FeOx$_{oxid}$ indicated poorly ordered Si-HFO as the only phase
197 (Fig. S7). It is important to note that LCF was performed with the independent components
198 representing Fh and Lp (Fig. S6). The spectrum of Si8-FeOx$_{oxid}$ is similar to that of Fh, but
199 the spectrum of P9-FeOx$_{oxid}$ has a very poorly developed corner-sharing Fe peak (Fig. 1).
200 This indicates that the structure of the P-rich Fe precipitate is different from Fh, which does
201 show a corner-sharing Fe peak. Indeed, previous work indicates that Fe precipitate formed by
202 Fe(II) oxidation in the presence of dissolved P consists of highly disordered Fe(III)-P
203 polymers and/or P-rich hydrous ferric oxide.[20-21] This material is less ordered than Fh, and
204 therefore an exaggerated relative concentatrion of Fh is needed in the LCF to reproduce the
205 relatively high degree of disorder in the P9-FeOx$_{oxid}$ spectrum. As poorly ordered Fe is
206 overestimated, the relative concentration of Lp in the sample is likely underestimated. Fitting
207 the P9-FeOx$_{oxid}$ spectrum with reference spectra for Lp and for highly disordered Fe(III)-P
208 polymers (obtained during previous work[21]) did not improve the quality-of-fit. This suggests
209 that the P-rich Fe precipitate on P9-FeOx$_{oxid}$ consisted of P-HFO rather than Fe(III)-polymers,
210 which is to be expected under the experimental conditions where the excess of Fe(III) over P
211 (P/Fe = 0.1) was large enough to drive polymerization of Fe(III)-P to P-HFO during
212 synthesis.[20]

213

A P9-FeOx$_{oxid}$ B Si8-FeOx$_{oxid}$

70% comp. 1 (Fh)
30% comp. 2 (Lp)

—— data
○ reproduced

100% comp. 1 (Fh)

k^{3}χ(k) (Å^{-3})

residual

residual

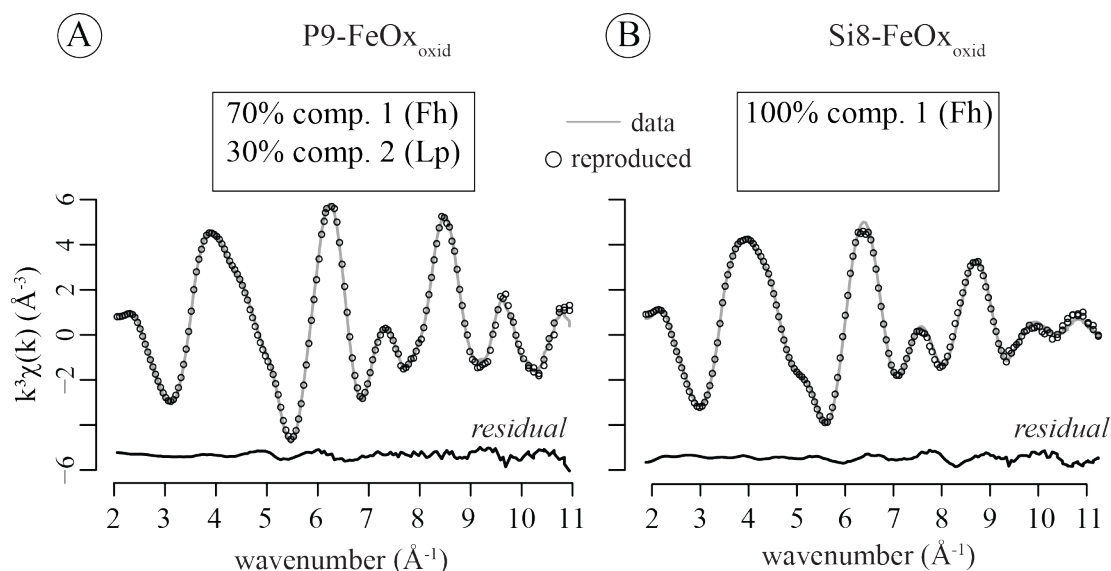wavenumber (Å^{-1})   wavenumber (Å^{-1})

214

215 **Figure S7**. Data (grey lines), reproduced spectra (black dots) and residuals (data - fit) for the
216 k^3-weighted Fe K-edge EXAFS data (fitting in k space, 2 - 11 Å^{-1}) of the FeOx starting
217 materials synthesized by Fe(II) oxidation with coprecipitation of P (P9-FeOx$_{oxid}$, panel A) or
218 Si (Si8-FeOx$_{oxid}$, panel B).

219

220 **LCF results for the Fe K-edge EXAFS spectra from Site 1 (freshwater) samples.**
221 Results of ITFA-LCF indicated that all spectra of samples from freshwater Site 1 were
222 reproduced as 100% poorly ordered FeOx. To look in more detail into Fe speciation in these
223 samples, we performed additional LCF in Athena, where sample spectra were reproduced as
224 linear combinations of spectra from reference materials rather than independent components
225 (Fig. S8). The results indicated that slight alteration of the starting material occurred in the
226 cases of P9-FeOx$_{hydr}$ and Si9-FeOx$_{hydr}$, even though all Fe remained present as poorly ordered
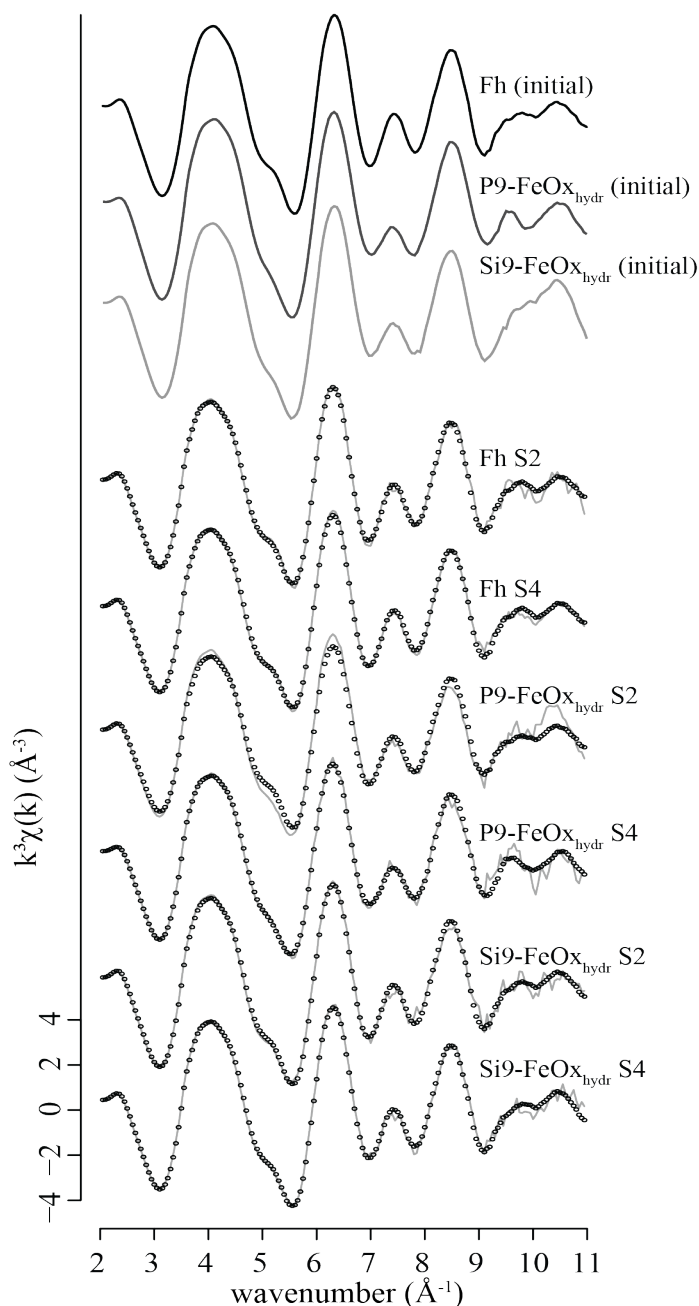227 FeOx (Table S1).

228

229 **Figure S8**. Data (grey line) and LCF fits (dots) (fitting k^3-weighted spectra in k space, 2 - 11
230 $Å^{-1}$) for the FeOx after four weeks of deployment in the freshwater sediment of Site 1. S2 is
231 section 2 of gel (3.5 - 7 cm) and S4 is section 4 of gel (10.5 - 14 cm). For each spectrum, the
232 two spectra of samples from duplicate probes were merged. For comparison, spectra of
233 starting materials are included at the top.

234

235 **Table S1**. Results of linear combination fitting of the Fe K-edge EXAFS data (fitting in χ
236 space, k 2 - 11 $Å^{-1}$) from the freshwater drainage ditch samples. Fractions were recalculated to
237 sum 1. S2 and S4 refer to the mid-depth (S2) and deepest (S4) sections of the deployed Fe-
238 MDT hydrogels. The standard deviation, representing the variability between samples from
239 duplicate probes, is between parentheses. Preliminary LCF with a suite of (mixed) ferric and
240 ferrous Fe phases such as lepidocrocite, goethite, hematite, magnetite, vivianite and siderite

241   showed that the contribution of these reference spectra to the sample spectra was negligible
242   (accounting for < 8% of total Fe in any combination of references).

	Fh S2	Fh S4	P9-FeOx$_{hydr}$ S2	P9-FeOx$_{hydr}$ S4	Si9-FeOx$_{hydr}$ S2*	Si9-FeOx$_{hydr}$ S4
P9-FeOx$_{hydr}$	-	-	0.00 (0.00)	0.73 (0.40)	-	-
Si9-FeOx$_{hydr}$	-	-	-	-	0.82	0.29 (0.04)
Fh	1.00 (0.01)	1.00 (0.01)	1.00 (0.00)	0.27 (0.37)	0.18	0.71 (0.05)
R factor**	0.028	0.015	0.039	0.039	0.019	0.020

243

244   * No duplicate available; no standard deviation

245   ** R factor is an estimate of the fitting error calculated as:

246     $sum((data - fit)^2) \big/ sum((data)^2)$ over the fitting range k = 2 - 11 Å^{-1}. Highest R factor of

247   duplicates is reported.

248

249

250

Dissolved sulfide and phosphate concentrations in marine sediment in the micro-cosm laboratory experiment. Pore-water profiles for DGT-DET showed accumulation of dissolved H_2S and P I the surface sediment. The DET gel for Fe(II) showed dark smears that precluded appropriate processing of the gel to obtain a Fe(II) map. Visual observation of areas of the gel that were not compromised, compared to the magenta color of the Fe(II) calibration series, indicated a transient Fe(II) peak of small magnitude (< 50 µmol L^{-1}) between $\sim$ 2–4 cm depth where H_2S was absent.

ΣH_2S (µmol L^{-1}) PO_4 (µmol L^{-1})

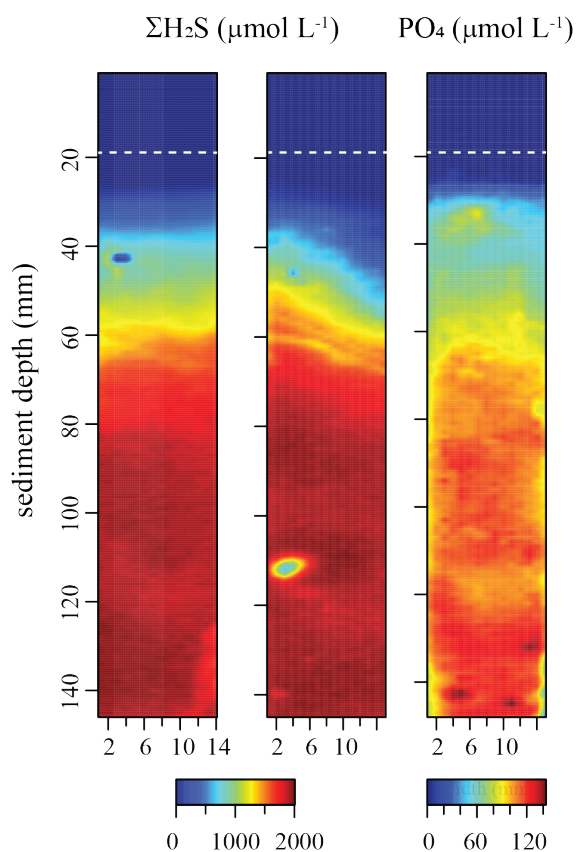**Fig. S9**. Dissolved ΣH_2S concentrations in the laboratory-based experiment with marine sediment from Site 2. Dashed white line indicates approximate position of sediment-water interface. The ΣH_2S concentrations were determined by DGT hydrogel. The passive samplers with DGT gels were deployed overnight, due to the high concentrations of dissolved ΣH_2S the sulfide binding agent likely was saturated. As such, the measurements in the lower parts of the gels represent underestimates; below $\sim$ 4 cm sediment depth the dissolved ΣH_2S concentration was at least 2 mmol L^{-1}.

Fe K-edge EXAFS spectra and ITFA-LCF results for samples from sulfidation experiment. The sample spectra and ITFA-LCF results are shown in Fig. S10, the relative contribution of the three components are listed in Table S2.
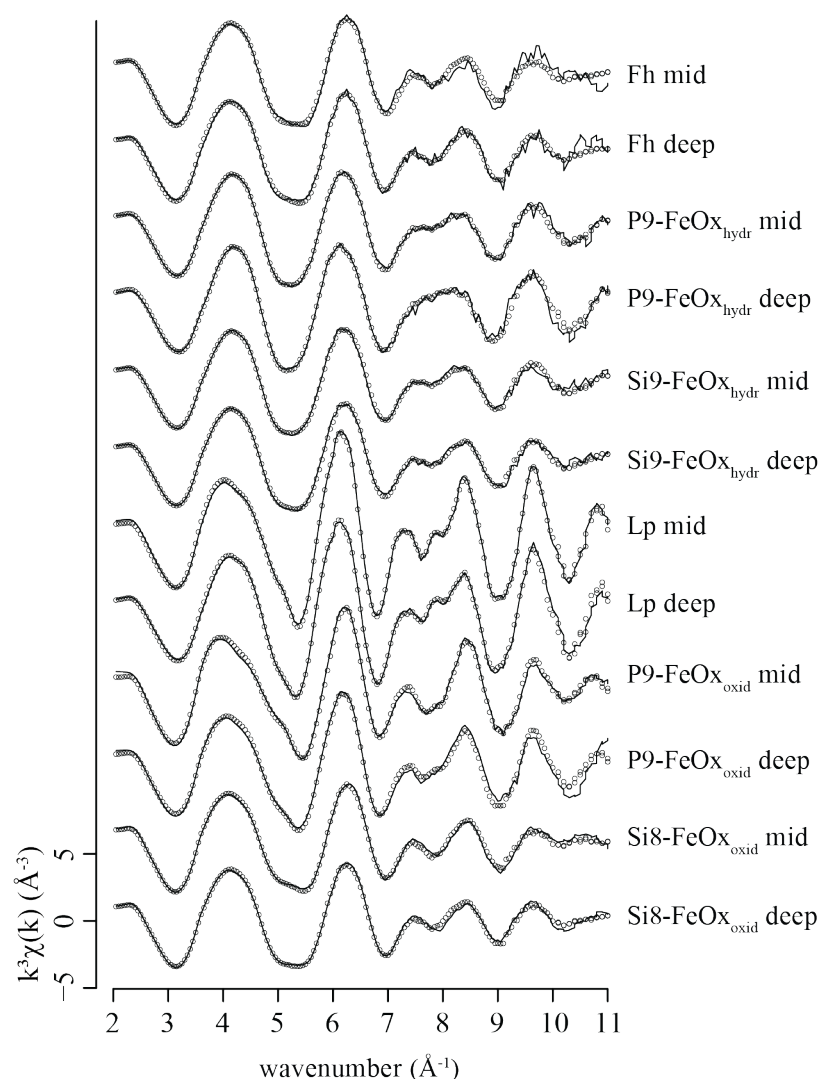

Fig. S10. Fe K-edge spectra of the samples from the microcosm sulfidation experiment (lines) and reproduction of the sample spectra using the three ITFA-derived components (dots). For each FeOx, gel sections 2 ("mid", 3.5–7 cm) and 4 ("deep", 10.5–14 cm) were analyzed.

Table S2. Weights of different ITFA-derived components in the reproduced spectrum. The Fe phase that each component represents is in parentheses. The weights represent the relative contributions of the different Fe phases (poorly ordered (P- or Si-bearing) FeOx, Lp and FeS).

Sample		comp. 1 (Fh)	comp. 2 (Lp)	comp. 3 (FeS)
1	Fh mid	0.75	0.00	0.25
2	Fh deep	0.72	0.03	0.25
3	P9-FeOx$_{hydr}$ mid	0.60	0.00	0.39
4	P9-FeOx$_{hydr}$ deep	0.47	0.00	0.53
5	Si9-FeOx$_{hydr}$ mid	0.65	0.00	0.35
6	Si9-FeOx$_{hydr}$ deep	0.68	0.02	0.30
7	Lp mid	0.02	0.54	0.43
8	Lp deep	0.06	0.36	0.58
9	P9-FeOx$_{oxid}$ mid	0.61	0.28	0.11
10	P9-FeOx$_{oxid}$ deep	0.45	0.24	0.32
11	Si8-FeOx$_{oxid}$ mid	0.82	0.01	0.18
12	Si8-FeOx$_{oxid}$ deep	0.75	0.00	0.25

Fe K-edge XANES results for samples from sulfidation experiment. The DOS was determined from ITFA-LCF that produced a component representing FeS as the only ferrous Fe phase (Fig. S4). As such, analysis of the Fe K-edge EXAFS data did provide evidence for a significant presence of non-sulfidized, excess Fe (see section 3.3.2). To furrther ascertain whether the XAS data provided any indication of excess Fe(II), we also analyzed the Fe K-edge XANES data. The positions of the Fe absorption edges (AEs) of (sulfur-bound) ferrous Fe phases lie at lower energies than the AE of ferric Fe phases (Fig. S11A). We used biotite, a ferrous Fe-bearing aluminosilicate, and siderite, Fe(II)CO$_3$, as representatives of fully reduced, non-sulfidized Fe. In addition, iron monosulfide and pyrite are used to represent ferrous Fe sulfide. Adapting an approach to use AE shifts for Fe speciation[22], we plot the energies at which the normalized AE of the different references is 0.5 ($E_{AE=0.5}$) (Fig. S11B). From this, we can discern that Fe(III) sulfidation results in a larger energy shift than Fe(III) reduction. We then tested for the presence of non-sulfidized excess Fe(II) by plotting $E_{AE=0.5}$ against DOS for samples from the lab-based sulfidation experiment. A large contribution of excess Fe(II) in addition to sulfidized Fe(II) would amplify the negative energy shift of the absorption edge, and consequently data points would plot below the sulfidation trendline. This is not observed: rather, data points plot close to or, particularly at lower DOS, slightly above the sulfidation trendline and align with the reduction trendline. Bearing in mind that caution has to be applied when interpreting such a small dataset, this could indicate that part of the energy shift for samples with relatively low DOS is in fact due to Fe(III) reduction rather than Fe(III) sulfidation (the former causes a smaller negative energy shift). The deviation from the sulfidation trendline is not observed for the samples with the highest DOS, which lends support to the idea that excess Fe(II) forms at the expense of FeS and is not observed when FeS formation is efficient (i.e. high DOS). We interpret these findings as tentative evidence for the presence of non-sulfidized Fe(II) in the samples from the sulfidation experiment. This would extend the model for different sulfidation pathways for FeOx based on batch laboratory experiments to natural sediments.
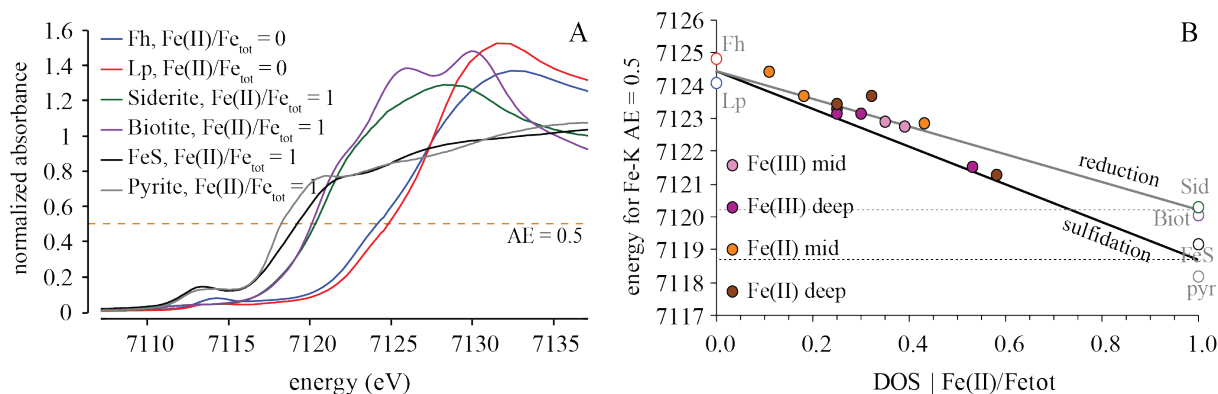
Fig. S11. (A) XANES spectra for selected ferric and ferrous references collected for this study and from a reference library collected at beamline 2-3 of the Stanford Synchrotron Radiation Lightsource (SSRL), kindly provided by Benjamin Kocar. The dashed orange line indicates normalized absorption edge (AE) = 0.5. (B) Energy at which AE = 0.5 ($E_{AE0.5}$) plotted against degree of sulfidation (DOS) or fraction of reduced Fe for ferric and ferrous references (white fill, color corresponding to colors in panel A) and for samples from the sulfidation experiment (filled circles). The solid black and grey lines represent the trend in $E_{AE=0.5}$ associated with progressive sulfidation or reduction of ferric FeOx, respectively. The horizontal dashed black and grey lines indicate the AE = 0.5 energies for spectra of fully sulfidized or reduced Fe, respectively. Mid and deep refer to mid-depth and deep gel sections analyzed in this study (see also Fig. 5).

References used

1. Michel, F. M.; Ehm, L.; Antao, S. M.; Lee, P. L.; Chupas, P. J.; Liu, G.; Strongin, D. R.; Schoonen, M. A. A.; Phillips, B. L.; Parise, J. B. The structure of ferrihydrite, a nanocrystalline material. *Science* **2007**, *316* (5832), 1726-1729.
2. Hiemstra, T. Surface and mineral structure of ferrihydrite. *Geochim. Cosmochim. Acta* **2013**, *105* (0), 316-325.
3. Schwertmann, U.; Cornell, S., *Iron oxides in the laboratory: Preparation and characterization*. Wiley: 1991; p 188.
4. Kraal, P.; van Genuchten, C. M.; Behrends, T.; Rose, A. L. Sorption of phosphate and silicate alters dissolution kinetics of poorly crystalline iron (oxyhydr)oxide. *Chemosphere* **2019**, *234*, 690-701.
5. Davis, C. C.; Chen, H.-W.; Edwards, M. Modeling Silica Sorption to Iron Hydroxide. *Environ. Sci. Technol.* **2002**, *36* (4), 582-587.
6. Swedlund, P. J.; Webster, J. G. Adsorption and polymerisation of silicic acid on ferrihydrite, and its effect on arsenic adsorption. *Water Res.* **1999**, *33* (16), 3413-3422.
7. Robertson, D.; Teasdale, P. R.; Welsh, D. T. A novel gel-based technique for the high resolution, two-dimensional determination of iron (II) and sulfide in sediment. *Limnol. Oceanogr. Meth.* **2008**, *6*, 502-512.
8. Davison, W.; Zhang, H. In situ speciation measurements of trace components in natural waters using thin-film gels. *Nature* **1994**, *367* (6463), 546-548.
9. Pagès, A.; Teasdale, P. R.; Robertson, D.; Bennett, W. W.; Schäfer, J.; Welsh, D. T. Representative measurement of two-dimensional reactive phosphate distributions and co-distributed iron(II) and sulfide in seagrass sediment porewaters. *Chemosphere* **2011**, *85* (8), 1256-1261.
10. Santner, J.; Prohaska, T.; Luo, J.; Zhang, H. Ferrihydrite containing gel for chemical imaging of labile phosphate species in sediments and soils using diffusive gradients in thin films. *Anal. Chem.* **2010**, *82* (18), 7668-7674.

346   11.   Stockdale, A.; Davison, W.; Zhang, H. High-resolution two-dimensional quantitative analysis
347   of phosphorus, vanadium and arsenic, and qualitative analysis of sulfide, in a freshwater sediment.
348   *Environmental Chemistry* **2008,** *5* (2), 143-149.
349   12.   APHA, *Standard methods for the examination of water and wastewater*. 21 ed.; American
350   Public Health Association - American Water Works Association - Water Environment Federation:
351   2005.
352   13.   Bennett, W. W.; Teasdale, P. R.; Welsh, D. T.; Panther, J. G.; Jolley, D. F. Optimization of
353   colorimetric DET technique for the in situ, two-dimensional measurement of iron(II) distributions in
354   sediment porewaters. *Talanta* **2012,** *88*, 490-495.
355   14.   Pages, A.; Teasdale, P. R.; Robertson, D.; Bennett, W. W.; Schafer, J.; Welsh, D. T.
356   Representative measurement of two-dimensional reactive phosphate distributions and co-distributed
357   iron(II) and sulfide in seagrass sediment porewaters. *Chemosphere* **2011,** *85* (8), 1256-61.
358   15.   Kelly, S. D.; Hesterberg, D.; Ravel, B., Analysis of soils and minerals using X-ray absorption
359   spectroscopy. In *Methods of Soil Analysis Part 5—Mineralogical Methods*, Ulery, A. L.; Drees, L. R.,
360   Eds. Soil Science Society of America: Madison, Wisconsin, 2008; Vol. SSSA Book Series.
361   16.   Nikitenko, S.; Beale, A. M.; van der Eerden, A. M. J.; Jacques, S. D. M.; Leynaud, O.;
362   O'Brien, M. G.; Detollenaere, D.; Kaptein, R.; Weckhuysen, B. M.; Bras, W. Implementation of a
363   combined SAXS/WAXS/QEXAFS set-up for time-resolved in situ experiments. *J. Synchrotron
364   Radiat.* **2008,** *15* (6), 632-640.
365   17.   Ravel, B.; Newville, M. Athena, Artemis, Hephaestus: data analysis for X-ray absorption
366   spectroscopy using IFEFFIT. *J. Synchrotron Radiat.* **2005,** *12*, 537-541.
367   18.   Rossberg, A.; Reich, T.; Bernhard, G. Complexation of uranium(VI) with protocatechuic
368   acid—application of iterative transformation factor analysis to EXAFS spectroscopy. *Anal. Bioanal.
369   Chem.* **2003,** *376* (5), 631-638.
370   19.   Kraal, P.; Burton, E. D.; Rose, A. L.; Kocar, B. D.; Lockhart, R. S.; Grice, K.; Bush, R. T.;
371   Tan, E.; Webb, S. M. Sedimentary iron–phosphorus cycling under contrasting redox conditions in a
372   eutrophic estuary. *Chem. Geol.* **2015,** *392* (0), 19-31.
373   20.   Voegelin, A.; Senn, A.-C.; Kaegi, R.; Hug, S. J.; Mangold, S. Dynamic Fe-precipitate
374   formation induced by Fe(II) oxidation in aerated phosphate-containing water. *Geochim. Cosmochim.
375   Acta* **2013,** *117*, 216-231.
376   21.   van Genuchten, C. M.; Peña, J.; Amrose, S. E.; Gadgil, A. J. Structure of Fe(III) precipitates
377   generated by the electrolytic dissolution of Fe(0) in the presence of groundwater ions. *Geochim.
378   Cosmochim. Acta* **2014,** *127*, 285-304.
379   22.   Shoenfelt, E. M.; Sun, J.; Winckler, G.; Kaplan, M. R.; Borunda, A. L.; Farrell, K. R.;
380   Moreno, P. I.; Gaiero, D. M.; Recasens, C.; Sambrotto, R. N.; Bostick, B. C. High particulate iron(II)
381   content in glacially sourced dusts enhances productivity of a model diatom. *Science Advances* **2017,** *3*
382   (6), e1700314.

383